Phenotypic and genetic spectrum of ATP6V1A encephalopathy: a disorder of lysosomal homeostasis

ATP6V1A developmental and epileptic encephalopathy: a disorder of lysosomal homeostasis

Renzo Guerrini[1], Davide Mei[1], Katalin Kerti-Szigeti[2], Sara Pepe[3,4], Mary Kay Koenig[5], Gretchen Von Allmen[5], Megan T. Cho[6], Kimberly McDonald[7], Janice Baker[8], Vikas Bhambhani[8], Zöe Powis[9], Lance Rodan[10], Rima Nabbout[11], Giulia Barcia[11], Jill A. Rosenfeld[12], Carlos A. Bacino[12], Cyril Mignot[13], Lillian H Power[14], Catharine J. Harris[15], Dragan Marjanovic[16], Rikke Steensbjerre Møller[17,18], The DDD Study[19], Riikka Keski Filppula[20], Päivi Vieira[21], Clara Hildebrandt[22], Stephanie Sacharow[23], Undiagnosed Diseases Network[24], Luca Maragliano[25,26], Fabio Benfenati[26,27], Katherine Lachlan[28], Andreas Benneche[29], Yue Si[6], Ingrid M. Wentzensen[6], Fanggeng Zou[6], Vinodh Narayanan[30], Naomichi Matsumoto[31], Alessandra Boncristiano[1], Giancarlo La Marca[32,33], Mitsuhiro Kato[34], Kristin Anderson[35], Carmen Barba[1], Luisa Sturiale[36], Domenico Garozzo[36], Roberto Bei[37], Laura Masuelli[38], Valerio Conti[1], Gaia Novarino[2], and Anna Fassio[27,39]

[1]Pediatric Neurology, Neurogenetics and Neurobiology Unit and Laboratories, Meyer Children's Hospital, member of ERN Epicare, University of Florence, Florence, Italy.
[2]Institute of Science and Technology (IST) Austria, Klosterneuburg, Austria.
[3]Department of Experimental Medicine, University of Genoa, Italy.
[4]Center for Synaptic Neuroscience and Technology, Istituto Italiano di Tecnologia, Genova, Italy.
[5]The University of Texas McGovern Medical School, Department of Pediatrics, Division of Child & Adolescent Neurology, Houston, Texas, USA.
[6]GeneDx, Gaithersburg, MD, 20877, USA.
[7]Pediatric Neurology, University of Mississippi Medical Center, Jackson, Mississippi, USA.
[8]Genetics and Genomics, Children's Minnesota, Minneapolis, Minnesota, USA.
[9]Ambry Genetics, Aliso Viejo, CA, USA.
[10]Division of Genetics and Genomics and Department of Neurology, Boston Children's Hospital, Harvard Medical School, Boston, MA, USA
[11]Reference centre for rare epilepsies, department of Genetics, Necker Enfants Malades hospital, APHP, member of ERN Epicare, Université de Paris, Paris, France.
[12]Department of Molecular & Human Genetics, Baylor College of Medicine, Houston, Texas, USA.
[13]APHP. Sorbonne Université, Départément de Génétique, Centre de Référence Déficiences Intellectuelles de Causes Rares, Paris, France & Institut du Cerveau (ICM), UMR S 1127, Inserm U1127, CNRS UMR 7225, Sorbonne Universite, 75013, Paris, France.
[14]Pediatric Neurology, Stead Family Department of Pediatrics, Unviersity of Iowa Stead Family Children's Hospital, Iowa City, Iowa, USA
[15]Department of Pediatric Genetics, University of Missouri Medical Center, Columbia, MO 65212, USA
[16]Danish Epilepsy Centre Filadelfia, Adult Neurology, Dianalund, Denmark
[17]Department of Epilepsy Genetics and Personalized Medicine, Danish Epilepsy Center, Filadelfia, Dianalund, Denmark
[18]Department of Regional Health Services, University of Southern Denmark, Odense, Denmark
[19]Wellcome Trust Sanger Institute, Hinxton, Cambridge, UK
[20]Department of Clinical Genetics, Oulu University Hospital, Medical Research Center Oulu and PEDEGO Research Unit, University of Oulu, Oulu, Finland.
[21]Clinic for Children and Adolescents, Oulu University Hospital, Medical Research Center Oulu and PEDEGO Research Unit, University of Oulu, Oulu, Finland.
[22]Division of Genetics and Genomics, Metabolism Program, Boston Children's Hospital, Boston, MA, USA.
[23]Boston Children's Hospital, Boston, MA, USA. & Harvard Medical School, Boston, MA, USA
[24]Harvard Medical School, Boston, MA 02115, USA

[25]Department of Life and Environmental Sciences, Polytechnic University of Marche, Ancona, Italy
[26]Center for Synaptic Neuroscience and Technology (NSYN@UniGe), Istituto Italiano di Tecnologia, Genova, Italy
[27]IRCCS Ospedale Policlinico San Martino, Genova, Italy
[28]Wessex Clinical Genetics Service, University Hospital Southampton NHS Foundation Trust, Southampton, UK & Human Development and Health, Faculty of Medicine University of Southampton, Southampton, UK.
[29]Department of Medical Genetics, Haukeland University Hospital, Bergen, Norway
[30]Neurogenomics Division, Center for Rare Childhood Disorders, Translational Genomics Research Institute (TGen), Phoenix, AZ 85012, USA.
[31]Department of Human Genetics, Yokohama City University Graduate School of Medicine, Yokohama Japan
[32]Newborn Screening, Clinical Chemistry and Pharmacology Lab, Meyer Children's University Hospital, Florence, Italy.
[33]Department of Experimental and Clinical Biomedical Sciences, University of Florence, Florence, Italy.
[34]Department of Pediatrics, Showa University School of Medicine and Epilepsy Medical Center, Showa University Hospital, Tokyo, Japan
[35]Founder & research liaison, "ATP6V1A Families" Facebook group
[36]CNR, Institute for Polymers, Composites and Biomaterials, IPCB, 95126 Catania, Italy
[37]Department of Clinical Sciences and Translational Medicine, University of Rome "Tor Vergata", Rome, Italy.
[38]Department of Experimental Medicine, University of Rome "Sapienza", Rome, Italy.
[39]Department of Experimental Medicine, University of Genoa, Italy

Address correspondence to:
Prof. Renzo Guerrini /
Tel: +39(0)555662573; Fax: +39(0)555662329; r.guerrini@meyer.it

Keywords: *epileptic encephalopathy, ATP6V1A, lysosomal homeostasis, lysosomal disorder, progressive brain atrophy, hypomyelination, developmental delay, induced neurons*

Abstract

V-type proton (H^+) ATPase (v-ATPase) is a multimeric complex present in a variety of cellular membranes that acts as an ATP-dependent proton pump and plays a key role in pH homeostasis and intracellular signaling pathways. In humans, 22 autosomal genes encode for a redundant set of subunits allowing the composition of diverse v-ATPase complexes with specific properties and tissue expression. Sixteen subunits have been linked to human disease. Here we describe 24 patients, harboring 19 distinct *de novo* missense *ATP6V1A* pathogenic variants, mainly clustering within the ATP synthase alpha/beta family, nucleotide-binding domain. Clinical presentations included early lethal encephalopathies with rapidly progressive brain atrophy, severe epileptic encephalopathies and mild intellectual disability with epilepsy. Using patients' fibroblasts and iPSC-derived neurons, we demonstrated abnormal lysosomal acidification and ultrastructure, associated with a significantly decreased lysosomal area. ATP6V1A-related developmental and epileptic encephalopathy represents a new paradigm among lysosomal disorders, as it results from a dysfunctional lysosomal membrane protein causing altered endolysosomal homeostasis. Its pathophysiology implies intracellular accumulation of substrates whose composition remains unclear, as well as the combination of structural brain abnormalities established early during prenatal brain development and progressive neurodegenerative changes, whose severity is variably determined by specific pathogenic variants.

INTRODUCTION

V-type proton (H^+) ATPase (v-ATPase) is a multimeric complex present in a variety of cellular membranes that acts as an ATP-dependent proton pump and is responsible for membrane trafficking processes, such as receptor-mediated endocytosis, intracellular trafficking of lysosomal enzymes, protein degradation, acidification of intracellular organelles in all eukaryotic cells, viral and toxin entry, bone resorption, pH homeostasis and tumor cell invasion (1, 2). The role of v-ATPase in pH homeostasis and intracellular signalling pathways is ubiquitous, but it is highly significant in neurons where it plays additional roles in neurotransmitter loading into synaptic vesicles and synaptic transmission (3, 4).

In humans, 22 autosomal genes encode for a redundant set of subunits allowing the composition of diverse v-ATPase complexes with specific properties and tissue expression. Among these, sixteen (*ATP6V0A1*, *ATP6V0A2*, *ATP6V0A3*, *ATP6V0A4*, *ATP6V0B*, *ATP6V0C*, *ATP6V0D1*, *ATP6V0D2*, *ATP6V1A*, *ATP6V1B1*, *ATP6V1B2*, *ATP6V1C1*, *ATP6V1E1*, *ATP6V1H*, *ATP6AP1*, *ATP6AP2*) have been associated with human disease (Supplemental Table 1).

In a previous study, we provided evidence that *de novo* heterozygous *ATP6V1A* pathogenic variants cause a developmental encephalopathy with epilepsy through a pathomechanism that involves the effects of v-ATPase in lysosomal homeostasis and neuronal connectivity (5).

Here, we provide evidence of the clinical spectrum of ATP6V1A encephalopathy through the description of 24 patients, harboring 19 different

de novo missense pathogenic variants clustering within the ATP synthase alpha/beta family, nucleotide-binding domain (ATP-synt_ab). Using patients' fibroblast and iPSC-derived neurons, we demonstrate how abnormal lysosomal homeostasis induces cell dysfunctions that predominate in the central nervous system, and whose clinical phenotype ranges from rapidly progressive early lethal encephalopathies to mild intellectual disability and epilepsy.

MATERIAL AND METHODS

Patients

We established a cohort of patients with pathogenic or likely pathogenic *ATP6V1A* variants from multiple diagnostic and research series from across Europe, the US and Japan. After our initial report associating *de novo* missense *ATP6V1A* pathogenic variants with a developmental and epileptic encephalopathy in four patients (5), the pathogenetic role of *ATP6V1A* variants was increasingly recognized in different centres and a group of families was established (https://www.facebook.com/groups/ATP6V1A/?ref=bookmarks), which helped in assembling the cohort presented here. This study includes the four patients described in our initial report together with 20 newly identified patients, of whom 18 are sporadic and two are monozygotic twins.

Genetic testing was performed using trio exome sequencing in all patients, in accordance with the respective national ethics guidelines and approved by the local authorities and ethic committees in the participating centres. The study was approved by the Pediatric Ethics Committees of the Tuscany Region, Italy,

in the context of the DESIRE FP7 EU project and its extension by the DECODE-EE project (see 'Acknowledgements' section at the end of manuscript).

Twenty-one patients (Pats. 1-10, 12, 13, 15-22, 24) were studied with repeated EEG recordings while awake and asleep. All patients had at least one brain MRI scan and 11 had at least a follow-up MRI (Pats. 1, 4, 5, 8-11 13, 15, 21 and 24). All patients' parents, or legal guardians, gave informed consent for genetic testing, skin biopsy, or both.

Genetic analysis and variant classification

All *ATP6V1A* variants were identified using trio exome sequencing (ES) primarily in the context of clinical diagnostic testing. The sequencing kits and technology varied according to the laboratories involved (see Supplemental Material), and the variants of interest were highlighted in the molecular diagnostic test reports. *ATP6V1A* variants were confirmed by Sanger sequencing in patients and their parents. All *ATP6V1A* variants were annotated based on canonical transcript (RefSeq NM_001690.3, Ensembl ENST00000273398.8, CCDS 2976.1). To assess the frequency of *ATP6V1A* variants in control populations, we used the population sequencing databases of the Exome Aggregation Consortium (ExAC) (http://exac.broadinstitute.org), the Genome Aggregation Database (gnomAD, v2.1.1) (http://gnomad.broadinstitute.org), the Human Genetic Variation Database (HGV) (http://www.hgvd.genome.med.kyoto-u.ac.jp) and BRAVO (TOPMed Freeze3a based on GRCh37/hg19; https://bravo.sph.umich.edu/freeze3a/hg19/). We used the Lollipops tool (6) to generate a lollipop diagram depicting *ATP6V1A* missense substitutions

identified in the 24 patients and reported in the ExAC dataset. We evaluated variants pathogenicity using a combination of *in silico* predictors available through the dbNSFP database v4.0 (https://sites.google.com/site/jpopgen/dbNSFP)(7). The *ATP6V1A* missense variants identified in patients and those reported in the gnomAD databases were extracted and annotated with dbNSFP 4.1a to compare seven established scores predicting variants deleteriousness (PolyPhen-2, SIFT, PROVEAN, CADD, M-CAP, MetaLR and MetaSVM). To further assess variant pathogenicity, we used the MPC (for Missense badness, PolyPhen-2, and Constraint) (8) and the MVP (for Missense Variant Pathogenicity) (9) scores for variant interpretation. We adopted these two tools in order to couple an approach exploiting the regional missense constraint (MPC) with another that was particularly performant in non-constrained genes (such as MVP). We classified and reported *ATP6V1A* variants according to the ACMG Laboratory Practice Committee Working Group guidelines (10). We also evaluated the likelihood for *ATP6V1A* to harbor dominant changes using the web server of the DOMINO tool (http://wwwfbm.unil.ch/domino) (11). *ATP6V1A* whole gene-level constraint was evaluated using the missense Z-score available in gnomAD v2.1.1 (12) and the Residual Variation Intolerance Score (RVIS) gene score based on ExAC v2 (13). Although gene-wide measures of constraint are effective for disease variant interpretation, metrics yielding a single score for an entire gene cannot capture the variability in regional constraint within protein-coding genes (14). To overcome this limitation we used the MTR-Viewer which quantifies the amount of purifying selection acting specifically on missense variants in a sliding window of 31 codons of protein-coding sequence calculated

using variation from more than 240000 exome and genome sequences (http://biosig.unimelb.edu.au/mtr-viewer) (15). We also used the map of constrained coding regions (CCRs) (14) to complement the constraint predictions made by both gene-wide and regional constraint metrics such as MTR.

We finally assessed genotype-phenotype correlations by comparing the locations of variants and the associated phenotypic features.

Structural modelling

To visualize the location of the mutated amino acids in the ATP6V1A structure and explore the impact of the distinct substitutions on the interaction of this subunit with other components of the vacuolar ATPase complex, we used the recently determined cryo-electron microscopy model of the rat brain protein (PDB accession code 6VQ9) (16) and the UCSF Chimera Visualization System (17).

Skin biopsy and fibroblasts cultures

Fibroblasts were derived from skin biopsies for Patients 1, 2, 11, 16, 18 and controls matched for sex, age at biopsy and passage in culture. Fibroblasts were cultured in DMEM (Thermo Fisher Scientific, Cat. # 41965-039) or RPMI (Life Technologies, Cat. # 21875-034) media supplemented with 20% fetal bovine serum (FBS, Gibco, Cat. # 10500-064) and 1% penicillin/streptomycin (Gibco, Cat #10378-016) at 37 °C in a humidified atmosphere with 5% CO_2.

Western blotting

Protein lysates from fibroblast cultures were extracted in lysis buffer (50 mM Tris [pH 7.4], 150 mM NaCl, 1 mM EDTA, 1% Triton X-100, 0.2 mM phenylmethylsulfonyl fluoride and 3 mM pepstatin), separated by SDS-PAGE and assayed by immunoblotting with anti-ATP6V1A (1/1000; #ab137574, Abcam) and anti-GAPDH (1/1000; #SC-25778, Santa Cruz Biotechnology) antibodies.

Immunocytochemistry and fluorescence microscopy

Fibroblasts were fixed in 4% paraformaldehyde and 4% sucrose in phosphate-buffered saline (PBS), permeabilized in 0.1% Triton X-100, blocked with 5% FBS in PBS and incubated with antibodies in blocking solution. Samples were mounted in ProLong Gold antifade reagent with DAPI (#P36935, Thermo-Fisher Scientific). Capture of confocal images was performed using a laser scanning confocal microscope (SP8, Leica) with 63X oil-immersion objective. For LAMP1 (1/200, #L1418 Sigma-Aldrich) labelling, each image consisted of a stack of images taken through the z-plane of the cell. For Lysotracker Deep Red (Lysotracker, Molecular Probes/Life Technologies) experiments, fibroblasts were incubated with 200 nM Lysotracker Deep Red for 1 h at 37 °C in culture medium, immediately fixed, stained with Alexa Fluor 546 phalloidin (1:40, #A22283 Thermofisher) and analyzed within 12 h. Images were taken at either epifluorescence (Olympus 1X81) or confocal (SP8, Leica) microscope in a single plane not to fade the fluorescent signal. Settings were kept constants for all acquisitions within each experiment.

Glycosylation analysis by MALDI TOF MS and MALDI TOF-TOF MS/MS

Transferrin was extracted from 120 µL of Patients 1 and 18 and controls serum samples by spin columns packed with IgY-derivatized microbeads (Seppro™ GenWay Biotech, San Diego, CA USA) as previously described (18), then deglycosylated by peptide N-glycosidase F (PNGase F, Roche Molecular Biochemicals, Mannheim, Germany).

Total N-glycan analysis was performed on 10 µL of serum samples after glycoprotein denaturation by RapiGest™ SF surfactant (Waters Corporation, Milford, MA, USA), reduction and alkylation by 5 mM dithiothreitol (DTT) and 15 mM iodoacetamide respectively, following by PNGase F deglycosylation. The released glycans, from either the whole serum or serum transferrin, were purified and permethylated prior to MS measurements (19). MALDI MS and MS/MS analyses were performed in positive polarity on a 4800 proteomic Analyzer (AB Sciex). An external calibration using a dedicated peptide calmix (AB Sciex) provided MS accuracy in reflector mode below 75 ppm. Data were processed using the DataExplorer™ software. The glycan profile of each patient was compared with a series of three age-matched controls and all the analyses were performed in triplicates.

Enzyme activity and biomarker analysis by LC-MS/MS

IDUA, GBA, GLA (GAA, GALC as controls) activities on sub-confluent fibroblasts were measured as previously described (20, 21). Briefly, fibroblasts cell pellet from Patients 1, 2, 11,16, and 18, were suspended in 100 µL of ULC/MS grade water (Biosove Chemie, Dieuze, France) and then sonicated in ice bath. The lysate was diluted 1:10 (v/v) with water (solution A) for the protein

content measurement (22). The assay was performed in triplicate. Three µL of the lysate were diluted 1:10 in 0.2% BSA (Merck Life Science Milan, cod. A9418) and incubated with an enzyme-specific cocktail at 37 °C for 22 h. After incubation, the reaction was stopped by adding 60 µL of ULC/MS grade methanol (Biosove Chemie, Dieuze, France), centrifuged to remove any suspended particles (2500 rpm for 3 min) and analyzed.

Glycosaminoglycans Heparan Sulfate (HS), Dermatan Sulfate (DS), Glucosylsphingosine (lyso-Gb1) and globotriaosylsphingosine (lysoGb3) were measured from solution A in triplicate using validated LC-MS/MS methods (23–25).

Generation of human induced pluripotent stem cells (iPSCs) and differentiation into induced neurons (iNs)

Fibroblasts obtained from two patients (Pats. 1 and 18) and a control subject (Control 1) were reprogrammed via non-integrating Sendai virus (SedV) according to the manufacturer's instructions (Cyto-Tune^{TM} IPS 2.0 Sendai Reprogramming Kit, Invitrogen). The induced pluripotent stem cell (iPSC) clones were tested for pluripotency by immunostainings for Nanog, Sox2, Oct3/4. After a few passages, the absence of SedV was tested with immunostaining with an anti-SedV antibody. The second control line (Control 2; iPSC) was a generous gift from the Tess Foundation (Chapel Hill, NC 27599, USA). iPSCs were cultured on Matrigel (Corning, NY, USA) coated 6-well plates in StemFlex medium (Thermo Fisher Scientific, MA, USA) and passaged twice per week.

Human iPSCs from Controls 1 and 2 and Patients 1 and 18 were differentiated into glutamatergic cortical layer 2/3 neurons by overexpressing the doxycycline-inducible transcription factor Neurogenin 2 (*Ngn2*) and rtTA via lentiviral vectors, as previously described (26, 27). Briefly, iPSCs were dissociated using Accutase (Sigma, Merck, Darmstadt, Germany) the day before transduction and plated on Matrigel coated 24-well plates (2.5 x 10^4 cell/well) in StemFlex medium supplemented with RevitaCell (Thermo Fisher Scientific, MA, USA) at 37 °C and 5% CO_2. The next day, cells were transduced with a mixture of Ngn2/rtTA lentiviruses (pLVX-(TRE-thight)-(MOUSE)Ngn2-PGK-Puromycin(R) and pLVX-EF1α-(Tet-On-Advanced)-IRES-G418(R)) generated by the Molecular Biology Services at IST Austria (Klosterneuburg, Austria). Media was changed 16 h later and cells were grown until they reached 80% confluency. Then, cells were dissociated and antibiotic selection with puromycin and G418 was initiated for at least 4-5 days. Antibiotic resistant clones for each iPSC line were picked in 96-well plates and expanded. Before inducing neuronal differentiation, iPSCs were dissociated with Accutase and plated in 6 well plates (3.5 x 10^5/well) to generate big batches of pre-differentiated cells (2 clones per subject). To induce differentiation, we cultured cells in KnockOut DMEM/F-12, N2-supplement and MEM NEAA (all from Thermo Fisher Scientific, MA, USA) supplemented with NT-3 (PeproTech; 10 ng/ml), BDNF (PeproTech; 10 ng/ml), laminin (Sigma; 1 ug/ml) and doxycycline (Sigma; 4 µg/ml). On the third day of differentiation, cells were frozen in 90% KOSR (Thermo Fisher Scientific) and 10% DMSO (Sigma). To generate induced neurons (iNs), pre-differentiated cells (1 x 10^5) were co-cultured with rat astrocytes at a 2:1 ratio on poly-l-ornithine/laminin (Sigma)-coated coverslips in a 24-well plate (DIV 0). Two iN

clones per subject (control and patient) were simultaneously generated. Cells were grown in BrainPhys Neuronal Medium (StemCell Technologies) complemented with 20% KOSR, 2% B-27 Plus supplement (Thermo Fisher Scientific), 0.2% Primocin (Invivogen) supplemented with NT-3 (10 ng/ml), BDNF (10 ng/ml), laminin (1 ug/ml) and doxycycline (4 ug/ml). The next day, media were changed completely and cytosine β-D-arabinofuranoside (Sigma) was added to a concentration of 2 μM to eliminate proliferating cells. From DIV 4, half of the medium was changed twice per week, and doxycycline treatment was stopped at DIV 8.

Transmission electron microscopy (TEM) of patients' fibroblasts

For ultrastructural analysis, cells were fixed in 2.5% glutaraldehyde in PBS, pH 7.4, at 4 °C, post-fixed in 1.33% osmium tetroxide, dehydrated in graded alcohol, transferred into toluene, and embedded in Epon 812 resin. Ultrathin sections of 90 nm thickness were stained with uranyl acetate–lead citrate and evaluated on a Philips transmission electron microscope Morgagni 268D (Philips, Endhoven, The Netherlands) according to our previously published protocol (28).

TEM of patients' iPSC-derived neurons (iNs)

Coverslips with co-cultures of human iNs and rat astrocytes at DIV 28 were fixed in 2.5% glutaraldehyde and 4% paraformaldehyde in PBS for 20 min at room temperature (RT). Samples were washed three times with PBS, and then processed using the high-contrast *en block* stain protocol to enhance the staining of neuronal membranes (29, 30). Briefly, samples were incubated in a

solution containing 1.5% potassium ferrocyanide and 2% osmium tetroxide in 0.1 M phosphate buffer (PB) for 1 h on ice in the dark. Coverslips were then washed in double-distilled water (ddH_2O) followed by incubation in thiocarbohydrazide solution for 20 min at RT. Subsequently, samples were rinsed in ddH_2O, and then placed in 2% osmium tetroxide in ddH2O for 30 min at RT in the dark. After extensive washing in ddH_2O, samples were incubated in aqueous 1% uranyl acetate overnight at 4 °C. The next day, samples were washed in ddH_2O prior to performing *en bloc* staining in Walton's lead aspartate solution for 30 min in a 60 °C oven. Next, samples were washed in ddH_2O and dehydrated in ascending series of ethanol. Finally, samples were infiltrated in propylene oxide followed by infiltration in 1: 2, 1: 1, and 2: 1 Durcupan resin: propylene oxide mixture for 1 hour each. Samples were then infiltrated in pure Durcupan resin and placed in a microwave (PELCO BioWave® Pro+) at 250 W under vacuum for 2 X 3 min. Coverslips were put on an ACLAR® foil and a BEEM capsule filled with fresh resin was placed on the center of the coverslip and allowed to polymerize for 48 hours at 60 °C. Fifty nm ultrathin sections were cut with an ultramicrotome (Leica Microsystems GmbH, EM UC7, Austria) with 4 mm Ultra 35° diamond knife (Diatome, Switzerland) and picked up on Pioloform coated slot grids. Images were taken with a transmission electron microscope (TEM, Tecnai 12, FEI/Thermo Fisher) with a side-mounted camera (OSIS Veleta) and analyzed with RADIUS software (EMSIS).

Neuronal cell bodies were randomly chosen, and 3X3, 4X4 or 5X5 electron micrographs were taken using the MIA function of the RADIUS software at either 26000X or 42000X magnification. Lysosomal areas were manually drawn, and their number and density were calculated in each measured cell

body area excluding the nucleus. All imaging and analyses were conducted with the experimenter blind to the analyzed condition.

Statistical analysis

Data are shown as means ± SEM or as medians with interquartile ranges with superimposed individual experimental points. Normal distribution was assessed using the Shapiro-Wilk normality test. To compare two normally distributed sample groups, the two-tailed unpaired Student's *t*-test was used. One-way ANOVA followed by either the Bonferroni's or the Tukey's multiple comparison test was used to compare more than two normally distributed sample groups. For non-normally distributed datasets, the Mann-Whitney *U*-test or the Kruskal-Wallis/Dunn's tests were used to compare two and more than two sample groups, respectively. A p-value <0.05 was considered significant. Data were analyzed using Prism8 (GraphPad Software).

RESULTS

Clinical, imaging, neurophysiological and genetic information on the 24 patients exhibiting *de novo ATP6V1A* pathogenic variants are summarized in Table 1 and presented in detail in the following sections.

Phenotypic spectrum

Mean age of the 24 patients at last follow-up was 7 years (extremes: 5 months for the youngest deceased patient – 22 years for the oldest living patient).

The most severe end of the phenotypic spectrum was manifested in three patients (Pats. 9, 13, and 15) who exhibited a profound, rapidly progressive

encephalopathy, manifested since birth with severe hypotonia and absence of any developmental skill, leading to early death in two of them (at 2 years in Pat. 9 and 5 months in Pat.15) (Table 1).

The most common first clinical manifestation in the cohort was early hypotonia, reported in 16 of the 22 patients (71%) for whom precise information on initial symptoms was available. In nine of the 16 infants with early hypotonia, seizures were also considered an initial symptom, as they were noticed at the same time. Nineteen/23 patients with available clinical information exhibited epilepsy (83%). Convulsive seizures during fever were an initial manifestation in seven of those with epilepsy (Pats. 1-4, 12, 21 and 22) and were not followed by epilepsy in one patient (Pat. 11). Based on epilepsy outcome and associated intellectual disability, we classified 15 patients who survived after early infancy as having a developmental and epileptic encephalopathy (DEE) (Pats. 1,4-8,10,17-24) (15/24, 62.5%; 15/20 with epilepsy, 75%; Table 1), whose onset was in infancy in 12 and in childhood in three (Pats. 8, 21 and 23). In the infantile onset DEE group, infantile spasms (IS) were the most prominent seizure type (10/12, 83% with EE; 10/20, 50% of all patients with epilepsy) and appeared at a median age of 7 months (range: 2 to 13 months). Additional myoclonic, tonic, tonic-clonic, atonic, absence and focal seizures were reported later in these children. In one of the three patients with childhood onset DEE (Pat. 8), intractable generalized tonic-clonic seizures appeared at age 7, followed by loss of acquired motor skills. All patients with DEE had been unsuccessfully treated with multiple antiepileptic drug trials.

Nine out of the 15 patients with DEE (Pats. 1, 4, 6, 7, 10, 17, 19, 20 and 24) exhibited early profound developmental delay with hypotonic quadriplegia and failed to achieve any developmental, communicative, or motor skill. The six remaining patients in this group (Pats. 5, 8, 18, and 21-23) acquired motor skills, which were subsequently lost in two of them after worsening of epilepsy (at 4 years Pat. 5) or after seizure onset (at 7 years Pat. 8). In this group, the only patients who acquired language skills, albeit poor, were the two whose epilepsy had started in childhood (Pats. 8 and 21). Mean age of the 15 patients with DEE at last follow-up was 6y6m (extremes: 10 months - 14 years).

The six remaining patients exhibited an association of intellectual disability (ID) and epilepsy (Table 1; Pats. 2, 3, 11, 12, 14, and 16; 6/24; 25%), which represented the mild end of the phenotypic spectrum. Intellectual disability was moderate in five patients and mild-moderate in one (Pat. 16); epilepsy was severe in two of these patients who, however, did not exhibit seizure-related progression of symptoms typical of EE. Different seizure types were diagnosed in this group, comprising generalized tonic-clonic (3/6), focal (2/6), myoclonic (1/6) and absence (1/6). One of these patients had only experienced rare seizures during fever (Pat. 11). The median age at seizure onset was 26 months (range: 15 months-3 years). All six patients achieved independent walking, and four acquired simplified language skills. Three exhibited mild autistic traits (Pats. 3, 12, and 16) and one an ADHD (Pat. 16). Mean age of these six patients at last follow-up was 10y6m (4-22 years).

Overall, language impairment was a highly prominent feature of this cohort since 12 of the 18 patients who were older than two years at last follow-up had remained nonverbal and six developed poor language skills.

EEG recordings were available for 22 patients, (Pats. 1-13, 15-22 and 24), 18 of whom with epilepsy (Pats. 1-8, 10, 12, 16-22 and 24). A hypsarrhythmic EEG was reported in two patients (2/20,10%; 2/20 with epilepsy, 10%), multifocal epileptiform discharges in ten (10/21, 48%;10/20 with epilepsy, 50%) and focal abnormalities in seven (7/21, 33%, 7/20 with epilepsy, 35%). Background EEG activity was described as abnormally slow in 11 patients (11/21, 52%), but we could not precisely correlate this finding with the clinical status of patients at the time of recordings.

Head circumference (HC) measures, at different ages, were available for 22/24 patients. Microcephaly (HC < -2SD) was present in eight patients (Pats. 1, 4, 9, 13, 14, 17, 19 and 24; 8/22: 36%), and could be demonstrated to be progressive in five (Pats. 1, 4, 13, 19 and 24). Head size measurements at birth revealed negative SD scores in 9/11 patients, while values < -1 SD were present in 13 patients (Pats. 1, 2, 4, 5, 7, 9, 11, 13-15, 17-19) and were already present in the first year of life in seven.

Amelogenesis imperfecta or enamel dysplasia were the definitions used in 7/24 patients (Pats. 2, 8, 11, 12, 14, 19 and 22; 29%) to describe these patients' combinations of eruption defects, defective enamel mineralization, and

excessive caries. Although information on dentition was not available for all patients, these findings were consistent and noteworthy.

Additional clinical manifestations included lack of visual contact (15/24, 63%), dyskinetic movements (4/24, 17%), optic atrophy and cerebellar signs (each present in 3/24 patients, 12.5 %), congenital arthrogryposis of joints (2/24, 9%), coloboma and dysmorphic features in one patient each. Four patients were G-tube dependent (Pats. 6, 7, 13, and 17; 17%).

Neuroimaging

Brain MRI was performed in 23/24 patients between age 1 week and 11 years and showed structural abnormalities in 19 (19/23; 83%) (Figure 1).

Abnormal MRI showed atrophic changes variably affecting the cerebral cortex (Pats. 1, 4, 6, 7, 9-11,13- 15, 17 and 24), brainstem and/or cerebellum (Pats. 1,5-8, 10-13, 15, 17 and 24), associated with dilated ventricles (Pats. 1, 4, 6, 7, 9, 10, 13, 15 17, and 24), thinning of the corpus callosum (Pats. 6, 7, 9, 12, 13, 15 and 24) and hypomyelination (Pats. 1, 4, 5-13, 15,18, 21 and 24).

In all eight individuals for whom repeated MRIs were available for comparison (Pats. 5, 8-11, 13, 15 and 24; Figure 1), there was worsening of atrophy, whose rate of progression and severity varied considerably. In Patients 9, 13 and 15, atrophy worsened dramatically within the first months of life, paralleling a clinical deterioration that eventually led to premature death in the first and second year of life in two of them (Pats. 9 and 15). The remaining five patients with follow-up imaging showed worsening of structural changes over longer periods, differently affecting brain and cerebellum (Figure 1). For example, in Patient 8 from age 1y6m to 7y6m, only mild cortical and cerebellar atrophy

became apparent. In Patient 11, instead, after a normal MRI at 11 months, mild cortical atrophy became apparent at repeat MRI scan at age 2y3m, while the cerebellum remained normal and hypomyelination persisted unchanged. Abnormal high signal intensity of the white matter, attributed to hypomyelination, was observed at any age and showed no signs of progression.

ATP6V1A whole gene-level constraint and predicted transmission model

The *ATP6V1A* whole gene-level constraint showed a positive missense Z-score of 3.37 (gnomAD v2.1.1) and an RVIS score (based on ExAC v2) of -1.041 (corresponding to the 11th percentile) suggesting an increased constraint and therefore intolerance to variations. The DOMINO tool assessed a high likelihood (0.911) for *ATP6V1A* gene to harbor dominant changes.

Genetic variants in ATP6V1A

The 24 patients harbored 19 unique heterozygous *ATP6V1A* variants (Table 1, Figure 2). Six variants had already been reported, of which four in our initial description of *ATP6V1A* encephalopathy (5), included as Patients 1-4, and two in patients listed in large cohorts with developmental disabilities, with limited clinical information (31, 32), included as Patients 14 and 17, with more clinical detail for Patient 17. The remaining 13 variants are novel. All 19 variants were *de novo* and missense; four substitutions were recurrent in unrelated patients (p.Pro249Arg Pats. 17 and 23; p.Arg359Gly Pats. 20 and 21; p.Pro375Thr Pats. 11 and 22; p.Arg381Pro Pats. 19 and 24), whereas one substitution (p.Gly276Arg) occurred in a monozygotic twin pair (Pats. 6 and 7). In four

unrelated patients, two distinct substitutions involved each of two residues (p.Asn314Ser/Asp and p.Pro412Ser/Leu), resulting in 17 different residues being involved in the overall series. None of the 19 missense substitutions was observed in the ExAC, gnomAD, HGV and BRAVO population databases (Supplemental Table 2). Predictions obtained from the dbNSFP database (v4.1a) were almost entirely concordant in defining a harmful impact on the ATP6V1A protein (Supplemental Table 3). The PolyPhen-2, SIFT, PROVEAN, CADD, M-CAP, MetaLR and MetaSVM *in silico* tools scores for ATP6V1A missense substitutions observed in patients and in gnomAD individuals, highlighted that all *de novo* variants identified in affected individuals cluster in the *deleterious* range for each score (Supplemental Figure 1). Both MPC and MVP scores obtained from patients' variants were significantly different from those observed in ExAC controls (Mann–Whitney's *U*-test; MPC p-value = 4.8×10^{-9} and MVP p-value=2.2×10^{-6}), as illustrated in the box-plot graphs (Supplemental Figure 2). Overall, these findings consistently supported a deleterious effect of the 19 variants.

We compared the presence and location of the 19 missense variants occurring in the 24 patients to those reported in the ExAC population database using a lollipop diagram depicting the full ATP6V1A protein and its Pfam-identified domains (Figure 2). The protein contains three Pfam conserved domains; ATP-synt_ab_N (from AA 21 to 83), ATP-synt_ab_Xtn (AA 99 to 221) and ATP-synt_ab (AA 230 to 455).

Analysis of the impact of these 19 variants, based on regional depletion in the general population using the MTR-Viewer tool, indicated that MTR scores were above the neutrality threshold for one ATP6V1A residue (Pat. 4 – Pro27

residue), above the 50th percentile (median), but below the neutrality threshold for five residues (Pat. 1 – Asp100, Pat. 5 – Gln103, Pat. 8 – Arg323, Pats. 11/22 – Pro375, Pats. 12/14 – Asn314); and below the median but above the 25th percentile for ten residues (Pat. 2 – Asp349, Pat. 3 – Asp371, Pats. 6/7 – Gly276, Pat. 10 – Leu345, Pat. 15 – Ser316, Pat. 16 – Gly363, Pats. 17/23 – Pro249, Pat. 18 – Glu356, Pat. 19 – Arg381, Pats. 20/21 – Arg359); one remaining residue (Pats. 9/13 – Pro412 residue) fell below the 5th percentile (Supplemental Figure 3).

Furthermore, we observed the regions with the lowest MTR scores, and therefore the highest intolerance to missense substitutions, to fall within the amino acid boundaries of the ATP-synt_ab domain (AA 230 to 455). Sixteen/19 substitutions were located in the ATP-synt_ab domain, suggesting its enrichment for pathogenic *ATP6V1A* variants (Figure 2). This domain is listed among the genome-wide significantly enriched domains for constraint (CCR: p-value of 0.0359; Bonferroni corrected across the 6,060 Pfam known domains) (14) (Supplemental Figure 4). The two remaining ATP6V1A Pfam domains, namely ATP-synt_ab_N and ATP-synt_ab_Xtn, were not significantly enriched for CCR (Supplemental Figure 4). The p.Pro412 residue involved in the missense substitutions (Pat. 9: p.Pro412Leu and Pat. 13: p.Pro412Ser) was located in one of the highly constrained *ATP6V1A* CCRs not covered by missense depletion (Hg19:chr3:113514042-113514777; 98.53 %ile)(14). Consistently with this observation, Patients 9 and 13 exhibited a strikingly similar phenotype with early onset rapidly progressive encephalopathy and profound brain atrophy (Figure 1).

Taken together, these findings strongly support pathogenicity of the *ATP6V1A* missense variants in this cohort and point to a pathogenics variants clustering within the ATP-synt_ab domain.

Structural consideration of the v-ATPase substitutions

We mapped the pathogenic variants we identified onto the recently published 3D structure of the rat ATP6V1A (PDB accession code 6VQ9)(16), which shares 98% sequence identity with the human protein. All substitutions but one (Pro27Arg, which maps in the N-terminal β-barrel domain) affect amino acids mapping in the N-terminal α/β, central domain surrounding the catalytic site (Figure 3 and Supplemental Video). The effect of p.Pro27Arg (perturbation of the ATP6V1A/B interaction), p.Asp100Tyr (destabilization of the protein folding), p.Asp349Asn (impairment of the catalytic function), and p.Asp371Gly (impairment of the rotation process) had been discussed previously (5). Among the newly identified substitutions, p.Pro249Arg, p.Pro412Leu/Ser, and p.Leu435Phe (Figure 3, red spheres) are located near the P-loop (residues 250-257), which includes the ATP binding site and may affect ATP/V-ATPase binding; p.Ser316Phe, p.Arg323Gly, p.Glu356Asp, p.Arg359Gly, and p.Gly363Val are at the interface between A and B subunits on the catalytic site side (Figure 3, yellow spheres), while p.Pro375Thr and p.Arg381Pro are at the interface between A and B subunits on the opposite side (the non-catalytic interface) (Figure 3, green spheres). All these pathogenic variants may perturb ATP6V1A/B interaction. The remaining substitutions (p.Gln103Arg, p.Asn314Asp/Ser, p.Gly276Arg) occur at sites whose structural characterization is less immediate (Figure 3, orange spheres). Gln103 is only

three positions away from Asp100, whose effect on the protein folding and degradation had been demonstrated previously (5) and confirmed here (Figure 4). Being surrounded by a cluster of hydrophobic residues, replacement of Gln103 with a bulkier, positively charged arginine is expected to strongly affect local amino acidic interactions. Asn314Asp substitution disrupts the H bond between the residue 314 and Cys277 (Supplemental Figure 5). In addition, this substitution determines that one of the carboxylic groups of Asp314 maps very close (about 2.7 Å) to the carboxylic group of Asp100 (Supplemental Figure 5). The Asn314Ser substitution is predicted to introduce an additional H bond between residue 314 and Cys277. Thus, although Asn314 does not map in a specific functional region of the protein, the Asn314Asp/Ser substitutions might affect local amino acidic interactions. Gly276 is about 5 Å away from the side chain of Asp349, which is in turn involved in the coordination of the Mg^{2+} ion at the ATP biding site (5). Hence, Gly276Arg is likely to perturb the catalytic site as well. In addition, Gly276 is one position away from Cys277, which was identified as the covalent target for EN6, a drug able to alter v-ATPase activity (33).

Glycosylation analysis

Serum glycosylation analyses were performed for Patients 1 and 18 by matrix-assisted desorption/ionization time-of-flight mass spectrometry (MALDI TOF MS). Transferrin N-glycan MS profiles showed mild abnormalities, consisting in a mild increase of the monosialo-biantennary glycoforms at *m/z* 2431.3 (A2G2S1) and 2605.5 (FA2G2S1) in both patients, and of the disialo-triantennary species at *m/z* 3241.7 (A3G3S2) and 3415.9 (FA3G3S2) for

Patient 18 and Patient 1, respectively. A general fucosylation increase, due to the enhancement of the monofucosylated structures normally present in human serum transferrin, was also observed in Patient 1 (data not shown).

Total serum N-glycan analysis reflected the same glycosylation defects (Supplemental Figure 6), with slightly increased hyposialylated and/or fucosylated structures in Patient 1 and increased amount of the biantennary monosialo-glycoforms A2G2S1 and FA2G2S1 in Patient's 18 glycosylation profile.

Transferrin N-glycan fucosylation was investigated in both patients by MALDI TOF-TOF MS/MS, with the purpose of discriminating core- from antennary fucosylated isoforms and establishing whether changes in the relative amount of the respective structures occurred. The fragmentation spectra of the most abundant fucosylated structure of patients' serum transferrin (namely FA2G2S2 at *m/z* 2966.5), revealed an about three-fold increase in the relative intensity of the antennary fucosylated isomer with respect to the reference range for controls, as showed in Supplemental Figure 7. MALDI MS analysis of serum apolipoprotein CIII (ApoCIII) was performed in Patient 1 and showed no obvious alterations of the mucin type O-glycosylation profile (data not shown).

Enzymatic activity and biomarker assay in fibroblasts

We measured enzymatic activity of Alpha-L-Iduronidase (IDUA), Alpha-galactosidase (GLA), Acid beta-D-glucosidase (ABG) in fibroblasts of Patients 1, 2, 11, 16, 18 and of two controls. We measured Acid alpha-glucosidase (GAA), Galactosyl-ceramidase (GALC) activities as internal controls. Patients had 56±15 - 240±42 % mean normal control activity for all three enzymes when

measured *in vitro* at optimal enzyme-specific pH. We quantified enzyme-specific natural substrates Heparan Sulfate (HS), and Dermatan Sulfate (DS) for IDUA, the Glucosylsphingosine (lyso-Gb1) for ABG and the globotriaosylsphingosine (lysoGb3) for GLA. DS was slightly increased in Patient 18 and decreased in Patients 1, 2, 11 and 16. The increment of HS was more evident (+69-240%) for all Patients except Patient 16. The lyso-Gb1 (+21-223%) and the lysoGb3 (+30-80%) where higher in all patients with respect to controls (Supplemental Table 4).

ATP6V1A expression and lysosomal labelling in patient-derived fibroblasts

We performed western blot and imaging analysis on subconfluent fibroblast cell cultures derived from Patients 1, 2, 16 and 18 and used fibroblasts from matched healthy individuals as controls. We first analyzed ATP6V1A protein expression and observed a significant decrease in fibroblast lysates from Patient 1, confirming previous findings in different cellular systems (5). No significant changes in ATP6V1A levels were observed for Patients 2, 16 and 18 (Figure 4A). We next evaluated the expression of the lysosomal marker LAMP1, and the organelle acidification process using the Lysotracker dye. We identified a decreased LAMP1 expression, accompanied by a lower Lysotracker staining, in fibroblasts of Patients 1 and 18 with respect to controls. Differently, fibroblasts of Patients 2 and 16 exhibited an increased Lysotracker staining, with no significant modification in LAMP1 expression (Figure 4B,C).

TEM studies in patient-derived fibroblasts

We performed ultrastructural analysis on subconfluent fibroblast cell cultures derived from Patients 1, 2, 16 and 18 and used fibroblasts of a healthy individual as control. Normal fibroblasts showed a thin and elongated appearance with centrally located nuclei and well-organized nucleoli (Figure 5A-C). Condensed mitochondria, slightly dilated endoplasmic reticulum and small lysosomes were observed in the cytoplasm. Conversely, fibroblasts from patients bearing *ATP6V1A* pathogenic variants showed several cytoplasmic single membrane-bounded vacuoles filled with heterogeneous substances, resembling lysosomal structures (Figure 5D-Q). The majority of vacuoles in fibroblasts from Patient 1 were packed with osmiophilic material and lamellated membrane structures resembling phospholipids (Figure 5D,E). In Patient 2's fibroblasts, the vacuolar structures were more heterogeneous and contained small electron dense granular materials in addition to lamellated membrane structures and osmiophilic material. Furthermore, few lipid droplets were visible in the cytoplasm (Figure 5G,H). In Patient 16's fibroblasts, vacuoles were packed with lamellated membrane structures and abundant lipid droplets were present (Figure 5L-N). In Patient 18's fibroblasts, vacuolar structures were very heterogeneous and filled with osmiophilic material and substances with different electron-density. Lipid droplets were also present (Figure 5O-Q).

Ultrastructural analysis of human IPSC-derived neurons (iNs) obtained from patients with ATP6V1A pathogenic variants

To study the morphological phenotype caused by *ATP6V1A* pathogenic variants in neuronal cells, we differentiated human glutamatergic neurons (iNs)

from induced pluripotent stem cells derived from fibroblasts of Patients 1 and 18, and two matched control subjects. iNs from both controls and patients showed MAP2 staining and immunoreacitivity for pre- and postsynaptic markers (Supplemental Figure 8). We then employed TEM analysis to study the ultrastructure of lysosomes in the iN somata of patients and control subjects. Electron dense lysosomes of various size and shape were often accumulated around the nucleus (Figure 6B, D) of iNs from both patients. We observed three types of lysosomes. Most of the lysosomes appeared as dark lamellar bodies, characterized by dense concentric lamellae inside their lumen (Figure 6B1-2, D1-2, F, G; lysosomes marked by *). Other lysosomes appeared as irregular structures, filled with dark and light material resembling lipid droplets (Figure 6B1, D2 lysosomes marked by #). A subset of lysosomes were small, round-shaped and filled with electron dense homogenous material (Figure 6D1, lysosomes marked by arrows). In contrast, neuronal somata from controls contained small to large mostly round lysosomes filled with homogenous material (Figure 6A1-2, C1-2, E).

To quantitatively assess the observed ultrastructural differences between patients' and controls' iNs, we quantified the number and area of lysosomes on electron micrographs of iN somata and found the area of lysosomes in patient-derived iNs to be significantly smaller compared to controls ($p<0.001$, Mann-Whitney *U*-test, Figure 6H). Additionally, compared to controls, in iNs from both patients we noticed a tendency towards an increased lysosome density (median with interquartile range (Q1-Q3): control = 0.32 (0.2-0.45) lysosomes/μm^2, n = 36 cells, 4 control samples (2 independent iN clones per control); patient = 0.35 (0.28-0.55) lysosomes/μm^2, n= 29 cells, 4 patient

samples (2 independent iN per patient); p = 0.12, Mann-Whitney *U*-test, Figure 6I).

DISCUSSION

This series of 24 patients with pathogenic *de novo ATP6V1A* variants defines the phenotypic spectrum of a dominant encephalopathy with variable severity. While rapidly progressive and early lethal phenotypes are seen at the most severe end of the spectrum, DEE with progressive worsening over several years form a *continuum* with milder static encephalopathies with intellectual disability and epilepsy which represent the milder end of the spectrum. Progression of symptoms, when present, had a variable speed. DEE can exhibit a relatively static course for years, or worsen at different ages, always resulting in a severe condition with no acquisition of communicative or motor skills. In the less severely affected group, including six patients, epilepsy and cognitive impairment were moderately severe, but none developed communicative language. Although no clear signs of progression were obvious in this group at the last follow-up (mean age 10y6m; range 4 - 22 years), a worsening course remains possible in the longer term.

Epilepsy was a main feature. Of the three patients with rapidly progressive neurodegenerative course (Pats. 9, 13, and 15), one died aged 5 months having had no seizures, another died at 2 years soon after seizure onset and the third has had no seizures at 25 months. These three patients faced very severe and rapid brain atrophy, a condition that may cause fading of synchronized electrical brain activity and, paradoxically, reduced

epileptogenesis. In the 19 remaining patients with epilepsy, multiple seizure types were observed with a clear prominence of early fever related seizures (8/23) and infantile spasms (9/23). Seizures were an initial symptom in 8/23, but were never considered as an isolated feature as they appeared in a context of early hypotonia (15/21) and developmental delay (all patients).

A small head size (< -1SD) could be demonstrated early in the course in 13/21 patients, reaching values consistent with microcephaly in at least 7/21. Although the randomness of head size measurements did not allow curves of head size growth to be precisely delineated, brain MRI showed signs of atrophy of brain and brainstem/cerebellar structures in 14/22 patients, accompanied by hypomyelination in most, or only hypomyelination in 2/22. All patients who had a repeat MRI scan, exhibited progressive atrophic changes, whose severity paralleled progression of symptoms. Clinical and imaging findings are consistent with a progressive neurodegenerative clinical course and indicate, in most patients, prenatal central nervous system impairment leading to symptoms onset early after birth or within the first year of life.

Abnormal dentition with enamel dysplasia, reported in seven patients, is consistent with similar observations in patients with autosomal recessive osteopetrosis (OMIM: #259700), caused by biallelic pathogenic variants of the *TCIRG1* gene, encoding the A3 subunit of the vacuolar (H^+) ATPase. V-type ATPase is significantly upregulated in enamel organ cells during maturation-stage (34) and the R740S/R740S V-ATPase A3 osteopetrotic mouse exhibits hypoplastic and hypomineralized enamel (35). In these animals, ameloblasts

contain numerous enlarged vacuoles, and osteoclasts have high lysosomal pH, which may interfere with proper enamel formation (35).

How do the 19 pathogenic variants described in the 24 patients possibly alter ATP6V1A function? The *ATP6V1A* gene is constrained to genetic variations as suggested by the gnomAD missense Z-score and the RVIS score and is predicted by DOMINO to be compatible with a dominant inheritance model, as we demonstrated in a previous study (5). Here, we strengthen the association of the *ATP6V1A* gene with a dominant encephalopathy by describing 24 patients 18 of whom, harboring 13 novel pathogenic variants, are newly reported (5, 31, 32). Overall, these 24 patients harbor 19 unique, and four recurrent, *de novo* missense substitutions not reported in the ExAC, gnomAD, HGV and BRAVO databases and predicted to be deleterious by *in silico* tools (PolyPhen-2, SIFT, PROVEAN, CADD, M-CAP, MetaLR and MetaSVM). MPC and MVP scores for these 19 pathogenic variants are significantly different from those observed for naturally occurring variants reported in ExAC database, which further supports pathogenicity. In addition, MTR scores based on regional depletion in the general population, highlighted a below-neutrality threshold for 18/19 residues affected by the *de novo* substitutions. The regions with the lowest MTR scores were observed in the ATP-synt_ab domain, known to be genome-wide significantly constrained (14). Sixteen/19 substitutions (84%) were located in this domain, suggesting an enrichment of pathogenic ATP6V1A variants in the ATP-synt_ab domain.

We previously mapped the four substitutions p.Pro27Arg, p.Asp100Tyr, p.Asp349Asn and p.Asp371Gly on the *E. hirae* crystal structure (PDB code 3VR6)(36), the *S. cerevisiae* Cryo-EM structure (PDB code 3J9T)(37), and a homology model of the human A subunit generated by us, showing that the variant sites are in the same locations in the three proteins (5). Recently, the Cryo-EM structure of a v-ATPase from *R. norvegicus* has become available (16). The subunit A of this enzyme shows 98% sequence identity with the human ATP6V1A, and its structure differs from our homology model by a root mean squared deviation (RMSD) of 2.8 Å (1.9 Å without considering the helical C-terminal domain). Therefore, the four substitutions analyzed in our initial study (5) are in the same locations also in the *R. norvegicus* ATP6V1A subunit, and we resolved to map the entire set of substitutions on this structure.

When mapped on the rat structure, most of the pathogenic variants (12 out of 19) resulted either close to the P-loop involved in ATP binding or in the A/B interface at the side of the catalytic site, thus possibly altering v-ATPase activity. Three other pathogenic variants mapped at the A/D and the non-catalytic A/B interface and could hence alter v-ATPase rotation or the interaction between subunits. The remaining four substitutions mapped in less specific regions of the protein but still appear to affect local amino acidic interactions in ways that could possibly result in decreased protein stability and expression. For Patient 1, bearing one of these pathogenic variants (Asp100Tyr), loss of expression of the ATP6V1A subunit was confirmed by western blot analysis, suggesting that in this patient (and possibly in all others harboring pathogenic variants affecting protein stability), an impaired expression is at the basis of the pathogenic process.

The number of patients carrying the various pathogenic variants is not sufficient to validate genotype-phenotype correlation with statistics. However, by correlating the position of the pathogenic variants in the rat ATP6V1A 3D structure with phenotype severity, we found that variants affecting protein folding, perturbing the catalytic site, or mapping near the P-loop containing the ATP binding site, are more frequently associated with severe phenotypes (Supplemental Table 5). In addition, a correlation between the specific amino acid substitution and phenotype severity can be assumed. Indeed, Patient 12, carrying the p.Asn314Ser substitution, exhibited a milder phenotype than Patient 14, carrying the more perturbing p.Asn314Asp substitution. The p.Pro412 residue, located in a highly constrained region of ATP-synt_ab domain and involved in the two different missense substitutions p.Pro412Leu and p.Pro412Ser (Pats. 9 and 13), resulted in profound phenotypes with early progressive severe brain atrophy.

Vacuolar-type ATPase is known to be expressed at lysosomal membranes to guarantee proper acidification of the degradative organelles for efficient enzymatic activity. Thus, acidification defects are usually linked with a progressive accumulation of non-degraded material inside lysosomes, a hallmark of lysosomal storage disease (LSD). Accordingly, ultrastructural analysis of fibroblasts from Patients 1, 2, 16 and 18 showed enlarged single membrane intracellular structures, reminiscent of autolysosomes, containing heterogeneous materials, with accumulated lipids among other degradative substrates. We further confirmed these findings in iPSC-derived iNs.

Particularly, in the somata of iNs from Patients 1 and 18, we found an accumulation of lysosomes with lamellar structures, lysosomes filled with dark and light material, resembling lipid droplets, and many small lysosomes filled with electron-dense material. In addition, we found that the area of lysosomes is significantly decreased in patients' iNs. Together with the ultrastructural diversity of iN lysosomes, this suggests that a functionally impaired ATP6V1A protein alters lysosomal maturation and function.

The overall clustering of the residues associated to pathogenic variants indicates that altered v-ATPase catalytic function or stability is at the basis of the abnormal phenotype and, together with ultrastructural data, clearly suggests the lysosomal nature of pathology. Fibroblasts of two severely affected patients (Pats. 1 and 18) exhibited reduced Lysotracker and LAMP1 labelling, suggesting that the filled structures observed by EM experience increased pH and reduced expression of the glycoprotein LAMP1. Reduced proton pump activity may result from both loss-of-function of the ATP6V1A subunit as a consequence of impaired catalytic activity (in line with the Glu356Asp pathogenic variant of Patient 18 mapping at the A/B interface at the catalytic side), or from loss of expression due to protein degradation (as demonstrated for the Asp100Tyr pathogenic variant in Patient 1). Impaired lysosomal acidification occurs in several progressive lysosomal disorders (38) and has been described in a patient with fulminant neurodegeneration carrying a *de novo* splice site pathogenic variant in the mammalian v-ATPase accessory factor *ATP6AP2* (39). Impaired lysosomal acidification with decreased Lysotracker signal was recently shown in cells expressing ATP6V0A1 missense

pathogenic variants, resulting in developmental encephalopathy with epilepsy (40). Fibroblasts of two less severely affected patients in our series (Pats. 2 and 16), exhibiting mild-moderate ID and epilepsy, revealed instead increased Lysotracker signal with no alteration of LAMP1 labelling. Although the molecular mechanism leading to the observed cellular phenotype needs further investigation, these findings suggest a decreased intralysosomal pH resulting from a v-ATPase gain-of-function. More acidic pH at intracellular organelles has been reported to similarly result in cytoplasmic inclusion with non-degraded materials due to reduced lysosomal hydrolase activity at the lowered pH, accumulation of aberrant lysosomal structures, or both (41). Hyperacidification of intracellular organelles has been associated with other neurodevelopmental disorders characterized by ID and seizures and caused by loss of function pathogenic variants in vesicular Na^+/H^+ exchanger genes (42).

Our data suggest that dominant pathogenic variants in *ATP6V1A* lead to defective autophagic and endocytotic lysosomal function, as a consequence of altered acidification. It is expected that in an altered environment, outside the 4-4.5 pH range, multiple enzymes operate sub-optimally leading to storage of the electron dense macromolecules which appear as lamellar and lipidic material in lysosomes of fibroblasts and IPSC-derived neurons. These findings are supported by the measurement of IDUA, ABG and GLA enzymatic activity. When the enzyme activity was measured *in vitro* after fibroblasts lysis and at optimal pH (3.4 for IDUA, 4.6 for GLA and 5.1 for ABG)(43, 44), no differences were observed between patients' and controls' cells. On the opposite, the biomarker's concentrations were higher in patients' than in controls' cells,

suggesting, with few exceptions, an *in vivo* sub-optimal catalytic environment that is not enzyme-specific.

Since lysosomes are also key players in cellular signalling and nutrient sensing, multiple cell compartments may suffer the downstream consequences of impaired lysosomal acidification. Mouse embryonic fibroblast lines obtained after v-ATPase inhibition or Atp6v1h silencing showed cellular iron deficiency, due to compromised iron release from lysosomes, resulting in impaired mitochondrial function and non-apoptotic cell death. These effects, accompanied by an inflammatory response, were also observed in a mouse model of impaired lysosomal acidification and were reversed by supplementation of the mouse diet with iron, which bypasses the endo-lysosomal pathway (45). Therefore, impaired lysosomal acidification may also result in an impaired iron homeostatic cycle and cause dysfunctional lysosomes to result in dysfunctional mitochondria.

Lysosomal disorders are caused by pathogenic variants in genes encoding lysosomal proteins, such as lysosomal glycosidases, proteases, integral membrane proteins, transporters, enzyme modifiers or activators (46). Most are inherited as autosomal recessive traits, and only three are X-linked. Therefore, biallelic or hemizygous pathogenic variants are necessary to cause disease via a critical reduction of the resulting enzymatic activity. In patients with heterozygous *ATP6V1A* pathogenic variants, however, the cumulative effects of the activity of multiple enzymes being simultaneously impaired are sufficient to cause disease. A homozygous form of ATP6V1A encephalopathy has been

observed in three patients from two consanguineous families, exhibiting *cutis laxa*, cardiac abnormalities, seizures, dysmorphic facial features, severe hypotonia, abnormal signal intensity, and polymicrogyria in one (47). In two of these patients, TEM of fibroblasts showed large heterogeneous vacuolar structures that the authors interpreted as similar to the large autolysosomes or lysosomal storage bodies seen in lysosomal-storage diseases. The authors also identified mildly impaired protein glycosylation and suggested v-ATPase defects to be, in part, a congenital disorder of glycosylation (CDG). Total serum and transferrin N-glycans profiles in Patients 1 and 18 in our series revealed minor changes due to a small increase of hyposialylated glycoforms, likewise reported in association with homozygous *ATP6V1A* pathogenic variants (47). In addition, transferrin-specific glycoform FA2G2S2 MS/MS analyses, revealed a substantial increase of the antennary fucosylation in both patients. Altered antennary fucosylation of plasma/serum glycoproteins has been documented in different diseases (48–50), including neurodevelopmental disorders (51). MS-based techniques enabling the identification and quantitation of antennary fucosylation are gaining primary interest, as it may reflect the total incidence of Lewis x/sialyl-Lewis x structural epitopes influencing glycoproteins functionality (52). We believe that the observed structural changes may represent a nonspecific outcome of the overall cellular disarrangement.

ATP6V1A is a lysosomal membrane protein, and ATP6V1A encephalopathy features seizures, intellectual disability and motor disorders in line with other diseases resulting from pathogenic variants affecting this protein category (46). ATP13A2 is also a lysosomal membrane protein, but disorders caused by pathogenic variants in its coding gene cause a form of recessive parkinsonism

with dementia of juvenile onset that is considered as a neuronal ceroid lipofuscinosis due to electron microscopy findings (46, 53). ATP13A2 has been established as a lysosomal polyamine exporter across lysosomes and early/late endosomes in neurons (54–56). Knockdown of the *Atp13a2* gene in cultured neurons causes accumulation and enlargement of lysosomes, decreased lysosomal degradation and accumulation of autophagosomes and alpha-synuclein (SNCA; OMIM: #163890), resulting in neuronal toxicity (57). A role for specific heterozygous *ATP13A2* variants in patients with early-onset Parkinson disease has been supported by rare reports and cellular studies (56). Pathogenic variants in other members/regulators of the v-ATPase complex have been recently described as causative for neurodevelopmental disorders and result in severely impaired brain development when modelled in mice (39, 40). In addition, in a multiomics profiling from cortical areas of patients with Alzhemer's disease, ATP6V1A deficit has been associated with neuronal impairment and neurodegeneration. In ATP6V1A silenced neurons, network activity was significantly reduced with increased immature spikes and alteration of synaptic proteins (Wang et al. 2021). This observation further suggests a role of ATP6V1A in neuronal maturation and activity, as we proposed for neurons expressing ATP6V1A pathogenic variants (5, 58).

In conclusion, ATP6V1A encephalopathy represents a new paradigm in the group of lysosomal diseases and should be considered as a lysosomal membrane protein disorder resulting in altered endolysosomal homeostasis. Its pathophysiology is complex, as it implies intracellular accumulation of substrates whose composition remains unclear, as well as the combination of

structural brain abnormalities that are established early during prenatal brain development and progressive neurodegenerative changes, whose severity is variably dictated by specific pathogenic variants.

AUTHOR CONTRIBUTIONS

Research study design: R.G., Da.Me., V.C., A.F. Acquiring and analyzing data: R.G., Da.Me., K.K.S., S.P., M.K.K., G.V.A., M.T.C., K.M.D., J.B., V.B., Z.P., L.R., R.N., G.B., J.A.R., C.A.B., C.M., L.H.P., C.J.H., Dr.Ma., R.S.M., R.K.F., C.H., S.S., Lu.Ma., F.B., K.L., An.Be., Y.S., I.M.W., F.Z., V.N., N.M., Al.Bo., G.L.M., M.K., K.A., C.B., L.S., D.G., R.B., La.Ma., V.C., G.N., A.F. Conducting experiments: D.M., K.K.S., S.P., G.L.M., L.S., D.G., R.B., La.Ma., V.C., G.N., A.F. Writing manuscript: R.G., D.M., Lu.Ma., F.B., Al.Bo., G.L.M., L.S., D.G., R.B., La.Ma., V.C., G.N., A.F.

ACKNOWLEDGEMENTS

We thank all patients and family members for their participation in this study. We thank Melanie Pieraks for generating the human iPSC lines, Vanessa Zheden and Daniel Gütl for their excellent technical support in the specimen preparation for TEM, and Flavia Leite for preparing the lentiviruses. The support from Electron Microscopy Facility and Molecular Biology Services at IST Austria is greatly acknowledged. We would like to thank Drs. Jane Hurst and Richard Scott for their help in retrieving the detailed clinical information of Patient 17. The research team acknowledges the support of the National Institute for Health Research, through the Comprehensive Clinical Research Network. See Supplemental Acknowledgments for Undiagnosed Disease Network

consortium details. Genetic information on Patient 23 was made available through access to the data and findings generated by the 100,000 Genomes Project; www.genomicsengland.co.uk (to K.L.).

This work was supported by the EU 7th Framework Programme (FP7) under the project DESIRE grant N602531 (to R.G.); the Tuscany Region Call for Health 2018 (grant DECODE-EE); IRCCS Ospedale Policlinico San Martino 5x1000 and Ricerca Corrente; This work is supported by the ERN for rare and complex epilepsies (EpiCARE). The DDD study presents independent research commissioned by the Health Innovation Challenge Fund [grant number HICF-1009-003], a parallel funding partnership between Wellcome and the Department of Health, and the Wellcome Sanger Institute [grant number WT098051]. The views expressed in this publication are those of the author(s) and not necessarily those of Wellcome or the Department of Health. The study has UK Research Ethics Committee approval (10/H0305/83, granted by the Cambridge South REC, and GEN/284/12 granted by the Republic of Ireland REC). This study makes use of DECIPHER (https://www.deciphergenomics.org), which is funded by Wellcome. K.K.S. was supported by the ISTplus fellowship.

CONFLICT OF INTEREST

J.A.R. and C.A.B. state that the Department of Molecular and Human Genetics at Baylor College of Medicine receives revenue from clinical genetic testing conducted at Baylor Genetics Laboratories. Y.S., I.M.W., and F.Z. are employees of GeneDx, Inc. Z.P. is a past employee of Ambry Genetics. The

remaining authors declare to have no conflict of interest related to the contents of this manuscript.

DATA AVAILABILITY

The authors confirm that the data supporting the findings of this study are available within the article and/or its supplementary materials. Further derived data supporting the findings of this study but not provided in the article due to space limitations are available from the corresponding author on request.

FIGURES AND LEGENDS

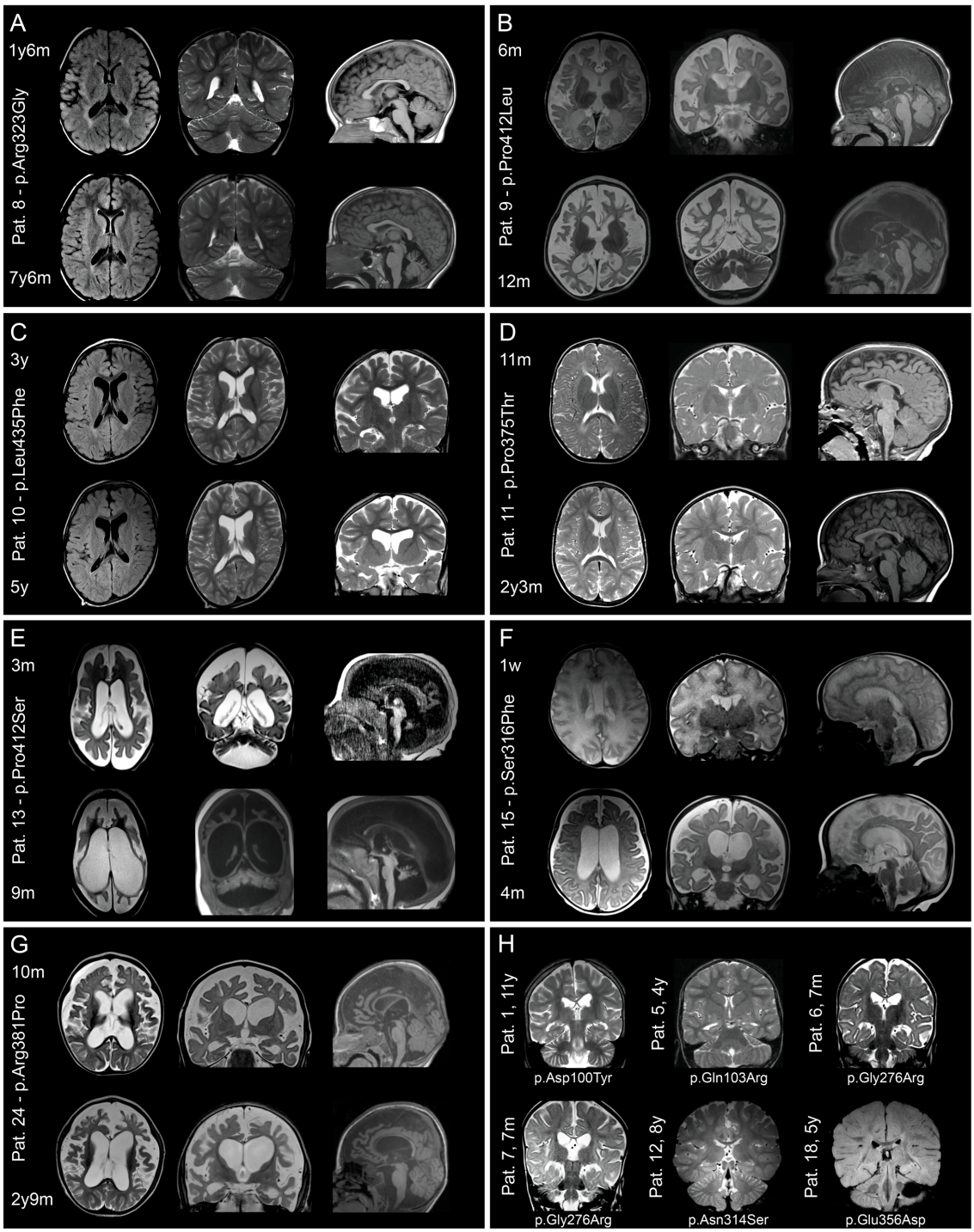

Figure 1. Brain MRI in patients with *ATP6V1A* pathogenic variants. MRIs of patients who were imaged at least twice are shown in A-G. Images were taken from the initial and last follow-up investigations at 1.5 to 3T and include

T1- or T2-weighted and fluid-attenuated inversion recovery sequences. Structural abnormalities include a combination of cerebellar and brainstem atrophy, dilated ventricles and subarachnoid spaces, thinning of the corpus callosum and hypomyelination. Comparison of initial and follow-up images demonstrates various rates of progression and anatomic involvement. In Patient 8 (A), at age 1 year 6 months, hypomyelination was the only feature, while cerebellar atrophy was present at 7 years 6 months. In Patients 9 (B) and 13 (E), MRI scan at age 6 months and 3 months, respectively, showed severe signs of atrophy that involved the cerebral cortex and white matter in Patient 9 and all brain, brainstem and cerebellar structures in Patient 13. Six months later, in Patient 9, at 12 months of age, atrophy had remarkably progressed, yet with minimal cerebellar involvement; in Patient 13, at 9 months, dramatic generalized shrinking of all brain structures had occurred. In Patient 15 (F), severe hypomyelination was present one week after birth followed, 4 months later, by severe brain atrophy. In Patient 24 (G) moderate brain atrophy with hypomyelination was present at 10 months, which became more severe 1 year and 11 months later. In Patients 10 (C) and 11 (D), mild atrophy became apparent from age 3 to 5 years (Pat. 10) and 11 months to 2 years 3 months (Pat. 11). Coronal sections of the brain of 6 patients who had only one MRI scan are presented in H. These images, taken at different ages, show hypomyelination in all patients and minor atrophic changes in two (Patients 6 and 7).

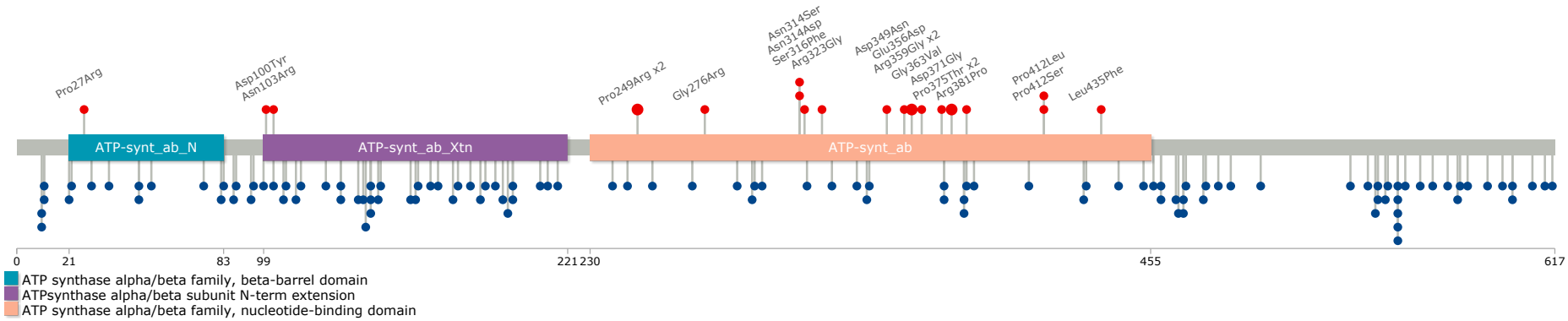

Figure 2. **Schematic representation of the ATP6V1A protein**. The structure of ATP6V1A includes the ATP-synt_ab_N (light blue), ATP_synt_ab_Xtn (purple) and ATP-synt_ab (light orange) domains. The red lollipops show the location of the pathogenic variants identified in the patients in this series, whereas the blue lollipops represent the missense variants reported in the ExAC database.

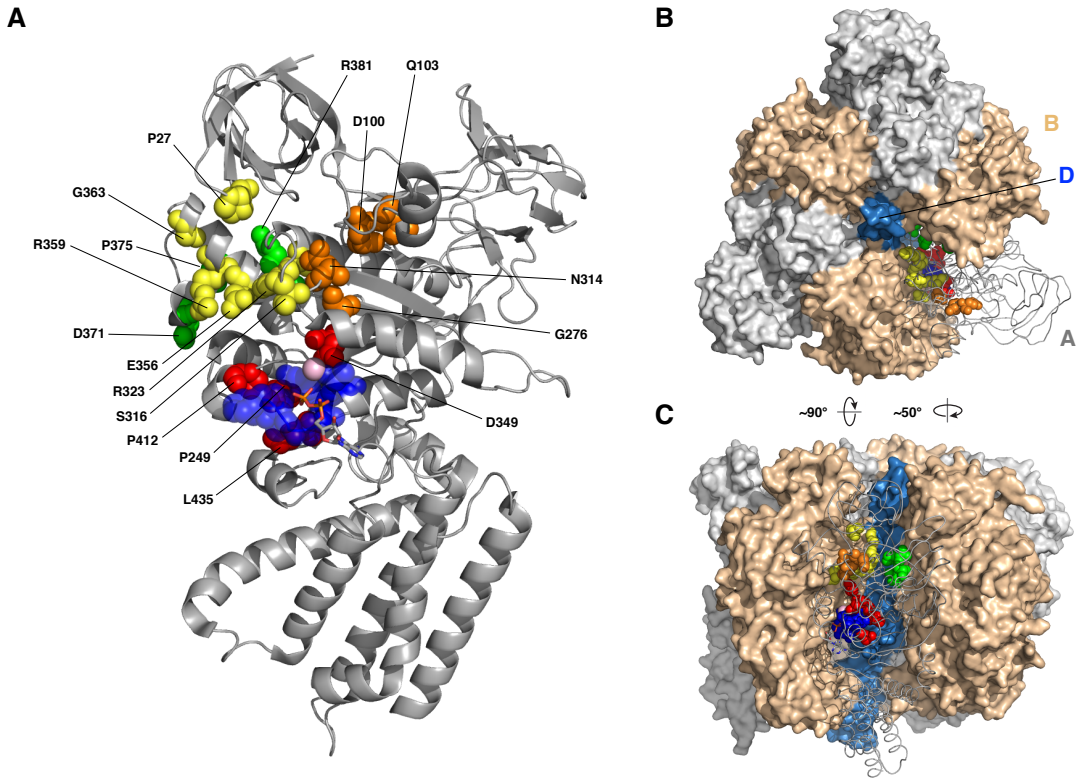

Figure 3. **Cryo-EM structure of the ATPV1A**. (A) The Cryo-EM structure of the A subunit from the mammalian v-ATPase (PDB code 6VQ9). Pathogenic variant sites are drawn as red, yellow, green and orange spheres if they are near the phosphate binding loop (p-loop, blue spheres), A/B interface, A/D or non-catalytic A/B interface, and uncharacterized locations, respectively. The pink sphere is the magnesium ion, and the bound ADP molecule is drawn as sticks. (B, C) Structure of the V1 domain from upper (B) and lateral (C) views. One A subunit is shown as grey tube and the other two as grey surface, and B and D subunits are shown as ochre and blue surfaces, respectively. Pathogenic variant sites are drawn as in (A).

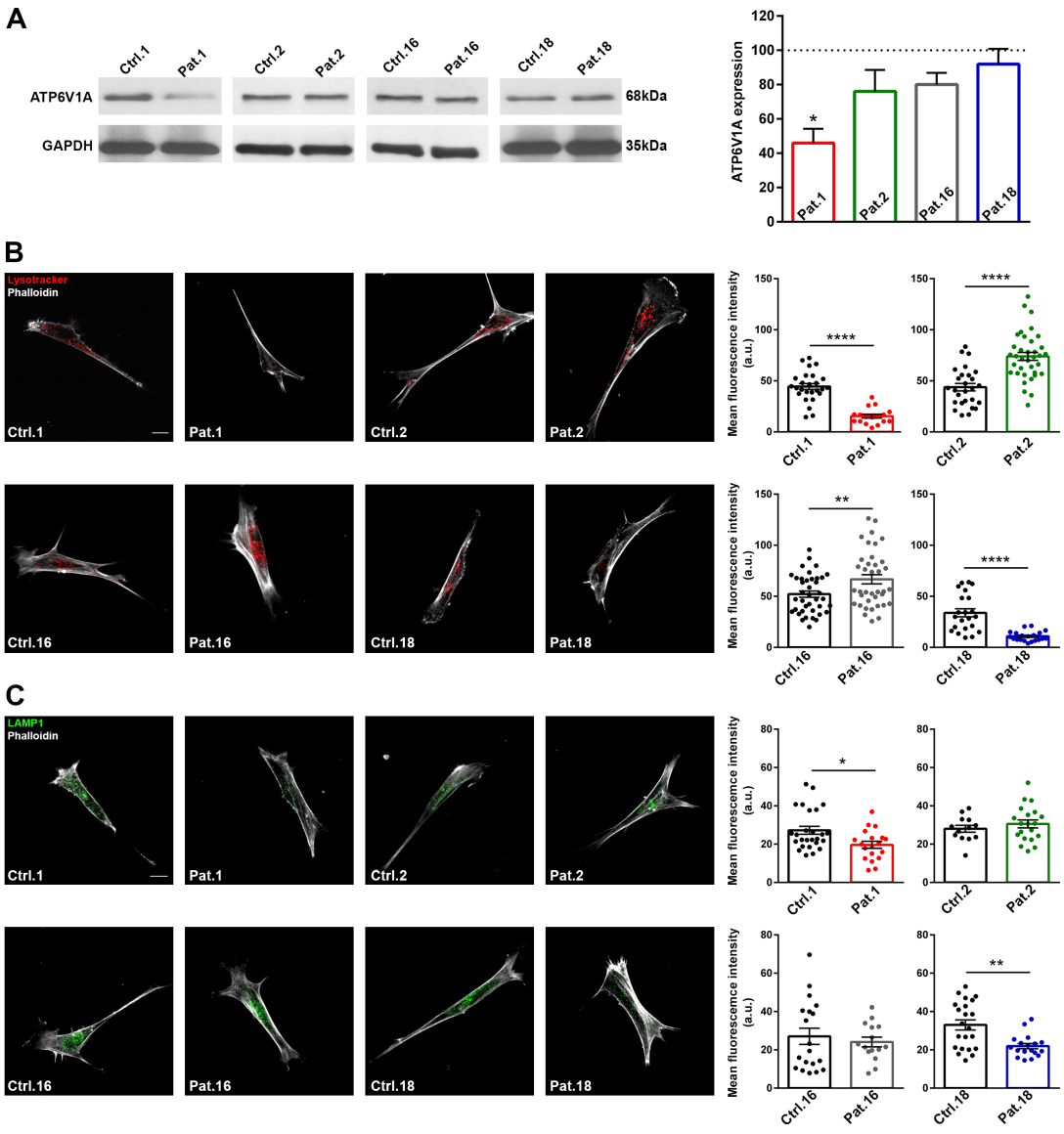

Figure 4. ATP6V1A/LAMP1 expression and LysoTracker phenotype. (**A**) *Left:* Representative western blots from fibroblast lysates of patients (Pats. 1, 2, 16 and 18) and the respective controls. *Right:* Quantification of ATP6V1A expression levels normalized on GAPDH signal and expressed, for each patient, as percentage of the respective control. Data are means ± SEM from five independent experiments for each patient. * p<0.05; Kruskal-Wallis/Dunn's tests. (**B**) *Left:* Representative images of fibroblasts incubated with Lysotracker and stained with phalloidin. Scale bar, 20 µm. *Right:* quantification of

Lysotracker intensity. The fluorescence signal was measured in the whole cell body identified by phalloidin staining. Each dot represents the mean fluorescence intensity of a cell. Data are means ± SEM from 26/17 cells for Ctrl.1/Pat.1, 27/36 cells for Ctrl.2/Pat.2, 39/38 cells for Ctrl.16/Pat.16, 22/20 cells for Ctrl.18/Pat.18. ** p<0.01, **** p<0.0001; unpaired Student's *t*-test. (**C**) *Left:* Representative images of fibroblasts double stained with LAMP1 and phalloidin. Scale bar, 20 µm. *Right:* Quantification of LAMP1 intensity. Immunoreactivity was measured in the whole cell body identified by phalloidin labelling. Each dot represents the mean fluorescence intensity of a cell. Data are means ± SEM from 26/19 cells for Ctrl.1/Pat.1, 13/20 cells for Ctrl.2/Pat.2, 19/15 cells for Ctrl.16/Pat.16, 22/18 cells for Ctrl.18/Pat.18. * p<0.05, ** p<0.01; unpaired Student's *t*-test/Mann-Whitney *U*-test.

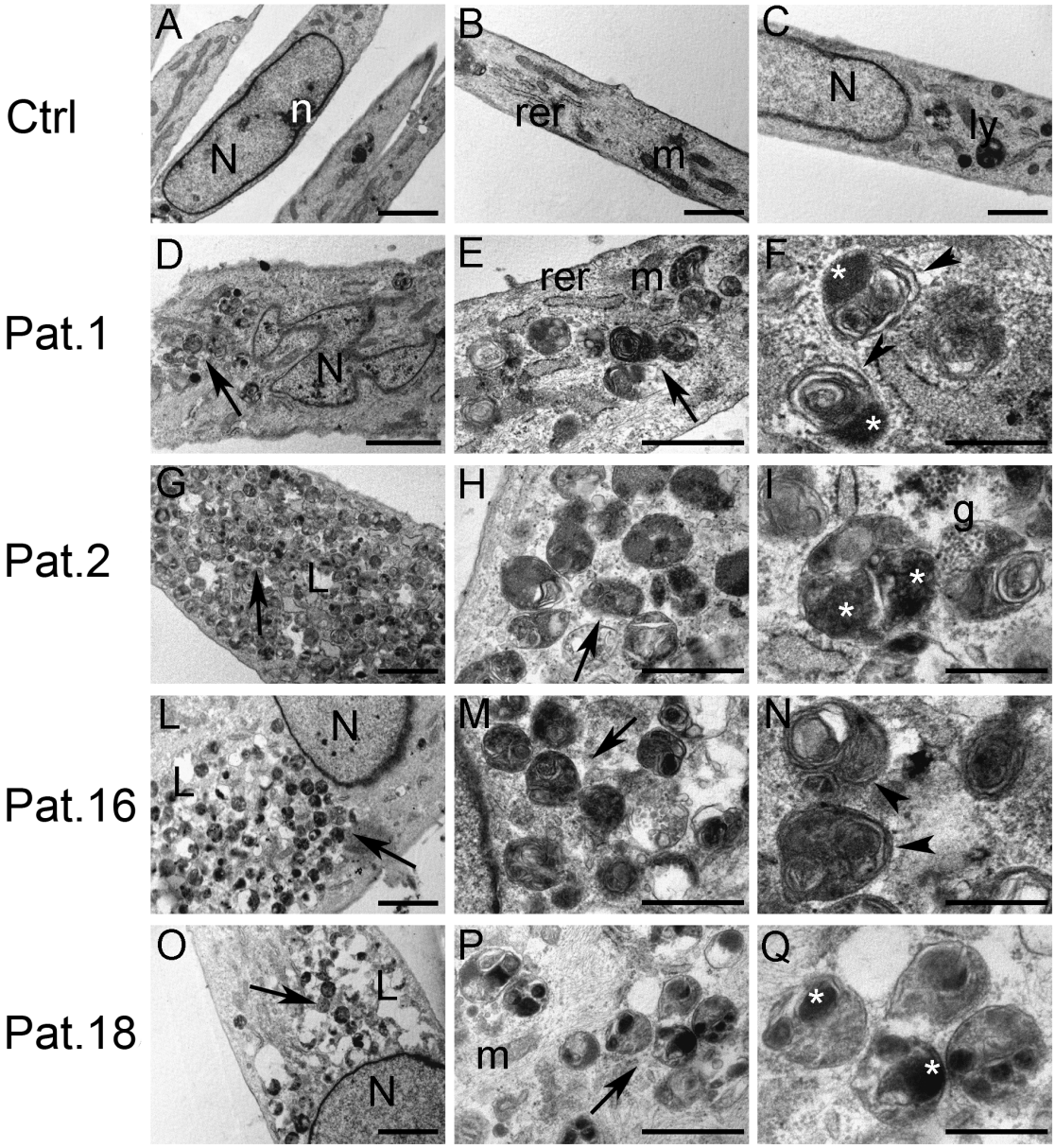

Figure 5. Ultrastructural analysis of fibroblasts derived from individuals with ATP6V1A pathogenic variants. (A-C) Control fibroblasts. (D-Q) Fibroblasts from patients Pat. 1 (D-E), Pat. 2 (G-I), Pat. 16 (L-N) and Pat. 18 (O-Q). Fibroblasts from patients bearing ATP6V1A pathogenic variants showed several cytoplasmic single membrane-bounded vacuoles filled with heterogeneous substances, resembling autolysosomes (arrows in D, E, G, H, L, M, O, P). Vacuoles from patients' fibroblasts were filled with various

substances, such as lamellated membrane structures (arrowheads in F and N), osmiophilic material (asterisks in F, I, Q), electrondense granular material (g in I) and substances with different electron-density (Q). N: nucleus; n: nucleolus; rer: rough endoplasmic reticulum; m: mitochondria; ly: lysosome; L: lipid droplets; arrows: cytoplasmic single membrane-bounded vacuoles; arrowheads: lamellated membrane structures; asterisks: osmiophilic material; g: electrondense granular material. Scale bars, 2 μm (A, D, G, L, O), 1 μm (B, C), 500 nm (E, H, M, P), 200 nm (F, I, N, Q).

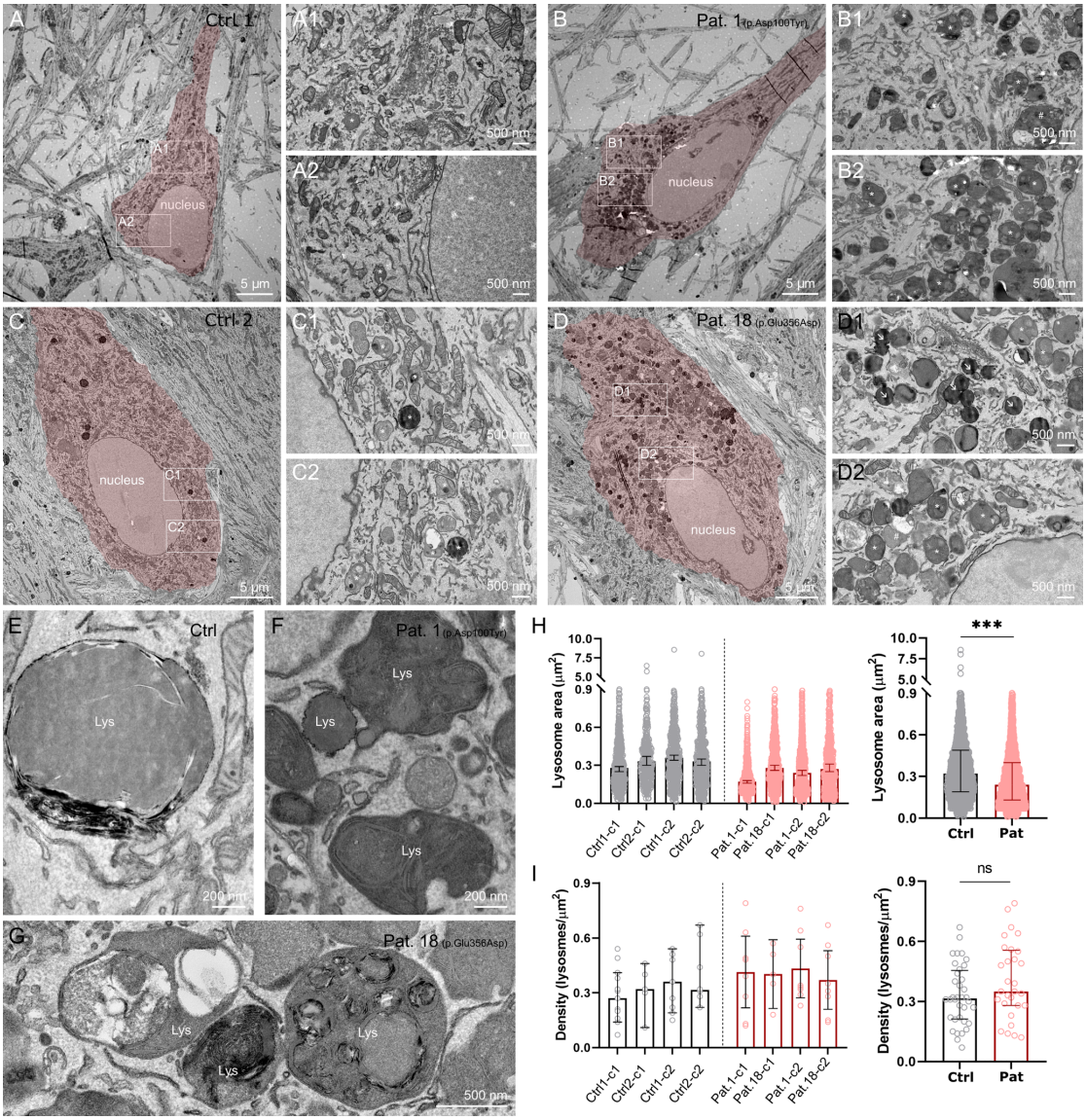

Figure 6. Ultrastructural analysis of patient-derived iNs. (A-D) Representative electron micrographs showing somata and proximal dendrites of control (A, C), Patient 1 (B) and Patient 18 (D) iNs (highlighted in red). (A1-2 and C1-2) High magnification images of the boxed regions in A and C, respectively. Asterisks (*) indicate lysosomes in control iNs. (B1-2 and D1-2) High magnification images of the boxed regions in B and D, respectively. Note the abundance of lysomes in Patient 1 (B) and Patient 18 (D) iN somata compared to control iNs. Asterisks (*) indicate lysosomes with dense concentric

lamellae, whereas # points to irregular shaped lysosomes filled with heterogeneous material and lipid droplets. (E) Large lysosome in control iNs. Note the homogenous and round structure of the organelle. (F) Lysosomes in the iN soma of Patient 1. (G) Lysosomes with heterogeneous material and lipid droplets in the iN soma of Patient 18. Note the irregular shape of lysosomes filled with concentric lamellae. (H, *left*) Lysosomal areas in iNs from control subjects and Patients 1 and 18 (N=2 independent iN clones per each subject). Data are presented as medians with 95% confidence intervals (CIs). (H, *right*) Pooled area of lysosomes for control and patient samples ($n_{control}$ = 2193 lysosomes from 4 samples; $n_{patient}$= 2918 lysosomes from 4 samples; $p < 0.001$, Mann-Whitney's *U*-test). Data are presented as medians with interquartile ranges (IQRs). (I, *left*) Density of lysosomes in iNs from control subjects and Patients 1 and 18 (N=2 independent iN clones per each subjects). Data are presented as medians with 95% CIs. (I, *right*) Pooled densities of lysosomes in control and patient samples ($N_{control}$ = 36 cells from 4 samples; $N_{patient}$= 29 cells from 4 samples; $p = 0.12$, Mann-Whitney's *U*-test). Data are presented as medians with IQRs. Lys: lysosome, Ctrl: control; Pat: patient; ns: not significant, *** $p < 0.001$.

REFERENCES

1. Forgac M. Vacuolar ATPases: Rotary proton pumps in physiology and pathophysiology. *Nat. Rev. Mol. Cell Biol.* 2007;8(11):917–929.

2. Cotter K et al. Activity of plasma membrane V-ATPases is critical for the invasion of MDA-MB231 breast cancer cells. *J. Biol. Chem.* 2015;290(6):3680–3692.

3. Morel N, Poëa-Guyon S. The membrane domain of vacuolar H(+)ATPase: a crucial player in neurotransmitter exocytotic release.. *Cell. Mol. Life Sci.* 2015;72(13):2561–73.

4. Bodzęta A, Kahms M, Klingauf J. The Presynaptic v-ATPase Reversibly Disassembles and Thereby Modulates Exocytosis but Is Not Part of the Fusion Machinery.. *Cell Rep.* 2017;20(6):1348–1359.

5. Fassio A et al. De novo mutations of the ATP6V1A gene cause developmental encephalopathy with epilepsy.. *Brain* 2018;141(6):1703–1718.

6. Jay JJ, Brouwer C. Lollipops in the Clinic: Information Dense Mutation Plots for Precision Medicine.. *PLoS One* 2016;11(8):e0160519.

7. Liu X, Wu C, Li C, Boerwinkle E. dbNSFP v3.0: A One-Stop Database of Functional Predictions and Annotations for Human Nonsynonymous and Splice-Site SNVs. *Hum. Mutat.* 2016;37(3):235–241.

8. Samocha KE et al. Regional missense constraint improves variant deleteriousness prediction. *bioRxiv* 2017;148353.

9. Qi H et al. MVP predicts the pathogenicity of missense variants by deep learning.. *Nat. Commun.* 2021;12(1):510.

10. Richards S et al. Standards and guidelines for the interpretation of sequence variants: a joint consensus recommendation of the American College

of Medical Genetics and Genomics and the Association for Molecular Pathology. *Genet. Med.* 2015;17(5):405–423.

11. Quinodoz M et al. DOMINO: Using Machine Learning to Predict Genes Associated with Dominant Disorders.. *Am. J. Hum. Genet.* 2017;101(4):623–629.

12. Lek M et al. Analysis of protein-coding genetic variation in 60,706 humans. *Nature* 2016;536(7616):285–291.

13. Gussow AB, Petrovski S, Wang Q, Allen AS, Goldstein DB. The intolerance to functional genetic variation of protein domains predicts the localization of pathogenic mutations within genes. *Genome Biol.* 2016;17(1):9.

14. Havrilla JM, Pedersen BS, Layer RM, Quinlan AR. A map of constrained coding regions in the human genome. *Nat. Genet.* 2019;51(1):88–95.

15. Silk M, Petrovski S, Ascher DB. MTR-Viewer: identifying regions within genes under purifying selection.. *Nucleic Acids Res.* 2019;47(W1):W121–W126.

16. Abbas YM, Wu D, Bueler SA, Robinson C V, Rubinstein JL. Structure of V-ATPase from the mammalian brain2020;1(March):1240–1246.

17. Pettersen EF et al. UCSF Chimera--a visualization system for exploratory research and analysis.. *J. Comput. Chem.* 2004;25(13):1605–12.

18. Sturiale L et al. Multiplexed glycoproteomic analysis of glycosylation disorders by sequential yolk immunoglobulins immunoseparation and MALDI-TOF MS.. *Proteomics* 2008;8(18):3822–32.

19. Messina A et al. CSF N-Glycoproteomics Using MALDI MS Techniques in Neurodegenerative Diseases.. *Methods Mol. Biol.* 2019;2044:255–272.

20. la Marca G, Casetta B, Malvagia S, Guerrini R, Zammarchi E. New strategy

for the screening of lysosomal storage disorders: the use of the online trapping-and-cleanup liquid chromatography/mass spectrometry.. *Anal. Chem.* 2009;81(15):6113–21.

21. Ombrone D et al. Screening of lysosomal storage disorders: application of the online trapping-and-cleanup liquid chromatography/mass spectrometry method for mucopolysaccharidosis I.. *Eur. J. Mass Spectrom. (Chichester, Eng).* 2013;19(6):497–503.

22. Smith PK et al. Measurement of protein using bicinchoninic acid.. *Anal. Biochem.* 1985;150(1):76–85.

23. Forni G et al. LC-MS/MS method for simultaneous quantification of heparan sulfate and dermatan sulfate in urine by butanolysis derivatization.. *Clin. Chim. Acta.* 2019;488:98–103.

24. Polo G et al. Plasma and dried blood spot lysosphingolipids for the diagnosis of different sphingolipidoses: a comparative study.. *Clin. Chem. Lab. Med.* 2019;57(12):1863–1874.

25. Malvagia S et al. Multicenter evaluation of use of dried blood spot compared to conventional plasma in measurements of globotriaosylsphingosine (LysoGb3) concentration in 104 Fabry patients.. *Clin. Chem. Lab. Med.* [published online ahead of print: April 29, 2021]; doi:10.1515/cclm-2021-0316

26. Frega M et al. Rapid Neuronal Differentiation of Induced Pluripotent Stem Cells for Measuring Network Activity on Micro-electrode Arrays.. *J. Vis. Exp.* [published online ahead of print: 2017];(119). doi:10.3791/54900

27. Zhang Y et al. Rapid single-step induction of functional neurons from human pluripotent stem cells.. *Neuron* 2013;78(5):785–98.

28. De Amicis A et al. Biological effects of in vitro THz radiation exposure in

human foetal fibroblasts.. *Mutat. Res. Genet. Toxicol. Environ. Mutagen.* 2015;793:150–60.

29. Deerinck T et al. Enhancing Serial Block-Face Scanning Electron Microscopy to Enable High Resolution 3-D Nanohistology of Cells and Tissues. *Microsc. Microanal.* 2010;16(S2):1138–1139.

30. Capetian P et al. Visualizing the Synaptic and Cellular Ultrastructure in Neurons Differentiated from Human Induced Neural Stem Cells-An Optimized Protocol.. *Int. J. Mol. Sci.* 2020;21(5). doi:10.3390/ijms21051708

31. Bosch DGM et al. Novel genetic causes for cerebral visual impairment.. *Eur. J. Hum. Genet.* 2016;24(5):660–5.

32. Deciphering Developmental Disorders Study et al. Prevalence and architecture of de novo mutations in developmental disorders.. *Nature* 2017;542(7642):433–438.

33. Chung CYS et al. Covalent targeting of the vacuolar H+-ATPase activates autophagy via mTORC1 inhibition. *Nat. Chem. Biol.* [published online ahead of print: 2019]; doi:10.1038/s41589-019-0308-4

34. Sarkar J, Wen X, Simanian EJ, Paine ML. V-type ATPase proton pump expression during enamel formation. *Matrix Biol.* 2016;52–54:234–245.

35. Johnson L et al. V-ATPases Containing a3 Subunit Play a Direct Role in Enamel Development in Mice. *J. Cell. Biochem.* 2017;118(10):3328–3340.

36. Arai S et al. Reconstitution in vitro of the catalytic portion (NtpA3-B3-D-G complex) of Enterococcus hirae V-type Na+-ATPase.. *Biochem. Biophys. Res. Commun.* 2009;390(3):698–702.

37. Zhao J, Benlekbir S, Rubinstein JL. Electron cryomicroscopy observation of rotational states in a eukaryotic V-ATPase.. *Nature* 2015;521(7551):241–5.

38. Colacurcio DJ, Nixon RA. Disorders of lysosomal acidification-The emerging role of v-ATPase in aging and neurodegenerative disease.. *Ageing Res. Rev.* 2016;32:75–88.

39. Hirose T et al. ATP6AP2 variant impairs CNS development and neuronal survival to cause fulminant neurodegeneration. *J. Clin. Invest.* 2019;129(5):2145–2162.

40. Aoto K et al. ATP6V0A1 encoding the a1-subunit of the V0 domain of vacuolar H+-ATPases is essential for brain development in humans and mice.. *Nat. Commun.* 2021;12(1):2107.

41. Nicoli E-R et al. Lysosomal Storage and Albinism Due to Effects of a De Novo CLCN7 Variant on Lysosomal Acidification.. *Am. J. Hum. Genet.* 2019;104(6):1127–1138.

42. Kondapalli KC, Prasad H, Rao R. An inside job: how endosomal Na(+)/H(+) exchangers link to autism and neurological disease. *Front. Cell. Neurosci.* 2014;8:172.

43. Li Y et al. Direct multiplex assay of lysosomal enzymes in dried blood spots for newborn screening.. *Clin. Chem.* 2004;50(10):1785–96.

44. Blanchard S, Sadilek M, Scott CR, Turecek F, Gelb MH. Tandem mass spectrometry for the direct assay of lysosomal enzymes in dried blood spots: application to screening newborns for mucopolysaccharidosis I.. *Clin. Chem.* 2008;54(12):2067–70.

45. Yambire KF et al. Impaired lysosomal acidification triggers iron deficiency and inflammation in vivo.. *Elife* 2019;8. doi:10.7554/eLife.51031

46. Platt FM, D'Azzo A, Davidson BL, Neufeld EF, Tifft CJ. Lysosomal storage diseases.. *Nat. Rev. Dis. Prim.* 2018;4(1):27.

47. Van Damme T et al. Mutations in ATP6V1E1 or ATP6V1A Cause Autosomal-Recessive Cutis Laxa. *Am. J. Hum. Genet.* 2017;100(2):216–227.

48. de Vroome SW et al. Serum N-glycome alterations in colorectal cancer associate with survival.. *Oncotarget* 2018;9(55):30610–30623.

49. Doherty M et al. Plasma N-glycans in colorectal cancer risk.. *Sci. Rep.* 2018;8(1):8655.

50. Thanabalasingham G et al. Mutations in HNF1A result in marked alterations of plasma glycan profile.. *Diabetes* 2013;62(4):1329–37.

51. Pivac N et al. Human plasma glycome in attention-deficit hyperactivity disorder and autism spectrum disorders.. *Mol. Cell. Proteomics* 2011;10(1):M110.004200.

52. Rebello OD et al. A novel glycosidase plate-based assay for the quantification of galactosylation and sialylation on human IgG.. *Glycoconj. J.* 2020;37(6):691–702.

53. Bras J, Verloes A, Schneider SA, Mole SE, Guerreiro RJ. Mutation of the parkinsonism gene ATP13A2 causes neuronal ceroid-lipofuscinosis.. *Hum. Mol. Genet.* 2012;21(12):2646–50.

54. van Veen S et al. ATP13A2 deficiency disrupts lysosomal polyamine export.. *Nature* 2020;578(7795):419–424.

55. Schultheis PJ et al. Atp13a2-deficient mice exhibit neuronal ceroid lipofuscinosis, limited α-synuclein accumulation and age-dependent sensorimotor deficits.. *Hum. Mol. Genet.* 2013;22(10):2067–82.

56. Podhajska A et al. Common pathogenic effects of missense mutations in the P-type ATPase ATP13A2 (PARK9) associated with early-onset parkinsonism.. *PLoS One* 2012;7(6):e39942.

57. Usenovic M et al. Identification of novel ATP13A2 interactors and their role in α-synuclein misfolding and toxicity.. *Hum. Mol. Genet.* 2012;21(17):3785–94.

58. Wang M et al. Transformative Network Modeling of Multi-omics Data Reveals Detailed Circuits, Key Regulators, and Potential Therapeutics for Alzheimer's Disease.. *Neuron* 2021;109(2):257-272.e14.